MEDIUM ENERGY NEUTRAL ATOM (MENA) IMAGER FOR THE IMAGE MISSION

C. J. POLLOCK[1], K. ASAMURA[2], J. BALDONADO[3], M. M. BALKEY[4], P. BARKER[3], J. L. BURCH[1], E. J. KORPELA[8], J. CRAVENS[1], G. DIRKS[1], M.-C. FOK[5], H. O. FUNSTEN[3], M. GRANDE[6], M. GRUNTMAN[7], J. HANLEY[1], J.-M. JAHN[1], M. JENKINS[1], M. LAMPTON[8], M. MARCKWORDT[8], D. J. MCCOMAS[3], T. MUKAI[2], G. PENEGOR[8], S. POPE[1], S. RITZAU[3], M. L. SCHATTENBURG[9], E. SCIME[4], R. SKOUG[3], W. SPURGEON[3], T. STECKLEIN[1], S. STORMS[3], C. URDIALES[1], P. VALEK[1,10], J. T. M. VAN BEEK[11], S. E. WEIDNER[1], M. WÜEST[1], M. K. YOUNG[1] and C. ZINSMEYER[1]

[1]*Southwest Research Institute, 6220 Culebra Road, San Antonio, TX 78238-5166, U.S.A.*

[2]*Institute of Space and Astronautical Sciences, 311 Yoshinodai Sagamihara, Kanagawa 229-8510, Japan*

[3]*Los Alamos National Laboratory, CSSE/NIS-1, Los Alamos, NM 87545, U.S.A.*

[4]*West Virginia University, Department of Physics, Box 6315, Morgantown, WV 26506, U.S.A.*

[5]*Universities Space Research Association, NASA GSFC, Greenbelt MD 20771, U.S.A.*

[6]*Rutherford Appleton Laboratory, Oxfordshire OX11 0QX, England*

[7]*University of Southern California, Department of Aerospace Engineering, Los Angeles, CA 90089, U.S.A.*

[8]*University of California at Berkeley, Space Sciences Laboratory, Centennial Drive at Grizzly Peak Blvd, Berkeley, CA 94720, U.S.A.*

[9]*MIT Center for Space Research, 77 Massachusetts Ave, Cambridge, MA 02139, U.S.A.*

[10]*Auburn University, Department of Physics, 206 Allison Laboratory, Auburn, AL 36849, U.S.A.*

[11]*Philips Research Laboratories, Prof. Holstlaan 4, 5656 AA Eindoven, The Netherlands*

(Received May 25, 1999)

Abstract. The Medium Energy Neutral Atom (MENA) imager was developed in response to the Imaging from the Magnetopause to the Aurora for Global Exploration (IMAGE) requirement to produce images of energetic neutral atoms (ENAs) in the energy range from 1 to 30 keV. These images will be used to infer characteristics of magnetospheric ion distributions. The MENA imager is a slit camera that images incident ENAs in the polar angle (based on a conventional spherical coordinate system defined by the spacecraft spin axis) and utilizes the spacecraft spin to image in azimuth. The speed of incident ENAs is determined by measuring the time-of-flight (TOF) from the entrance aperture to the detector. A carbon foil in the entrance aperture yields secondary electrons, which are imaged using a position-sensitive Start detector segment. This provides both the one-dimensional (1D) position at which the ENA passed through the aperture and a Start time for the TOF system. Impact of the incident ENA on the 1D position-sensitive Stop detector segment provides both a Stop-timing signal and the location that the ENA impacts the detector. The ENA incident polar angle is derived from the measured Stop and Start positions. Species identification (H vs. O) is based on variation in secondary electron yield with mass for a fixed ENA speed. The MENA imager is designed to produce images with $8^\circ \times 4^\circ$ angular resolution over a field of view $140^\circ \times 360^\circ$, over an energy range from 1 keV to 30 keV. Thus, the MENA imager is well suited to conduct measurements relevant to the Earth's ring current, plasma sheet, and (at times) magnetosheath and cusp.

Space Science Reviews **91:** 113–154, 2000.

1. Introduction

1.1. Scientific background and objectives

The IMAGE mission was conceived in response to the need to achieve instantaneous visualization of many of the major structures in the Earth's magnetosphere. Global visualization of the magnetosphere will add greatly to our understanding of its structure and the processes that link the magnetosphere with the exterior solar wind and the Earth's atmosphere and ionosphere. The case was made eloquently by Williams et al. (1992) in their comprehensive review of magnetospheric imaging. Here we have a classic case of a picture being worth a thousand words. In this analogy, each of those 'thousand words' may be thought of as an isolated observation by an in situ spacecraft. The ensemble of such observations at points separated in both space and time has, for the most part, formed the basis of our current understanding of magnetospheric structures and processes. Sampled at one or a few widely separated places, these data have formed a very large, yet still sparse, array of constraints on the system under study. This paper describes the measurement technique of the Medium Energy Neutral Atom (MENA) imager that, as part of the IMAGE mission, will enable global observation of magnetospheric structure and dynamics using images of the magnetosphere in energetic neutral atoms (ENAs). The images will not be photographs. Rather, we may call them 'enagraphs'.

A body of work in magnetospheric imagery that has had large scientific and public impact is that of auroral imaging from space. Though preceded and followed by several space-based auroral imagers, the first planetary scale images of the aurora were presented to the world with the launch of the DE-1 spacecraft (Frank et al., 1981, 1982). The utility of global auroral imaging for the study of magnetospheric physics is difficult to overstate. The technique is used to monitor the spatio-temporal evolution of substorms, discern spatial relationships in highly dynamic contexts, estimate global ionospheric energy deposition, and to understand important aspects of the magnetosphere's morphology. Nevertheless, auroral imaging is limited since global dynamics are interpreted through their effects on the aurora. With the MENA instrument we can directly observe global structure and dynamics.

In situ magnetospheric data products are epitomized by energy-time particle flux spectrograms and frequency-time field spectrograms obtained along spacecraft trajectories. Space physicists have developed intuition unique to these data displays, such that profound physical understanding has been obtained through careful consideration and analysis of such products. However, single point measurements do have some limitations, which the IMAGE mission has been designed to address:

1. Causality: The traditional data of magnetospheric physics, coupled with knowledge of plasma physics, are well suited for use in characterizing various populations and processes resident in the magnetosphere. However, the physical dimensions (particle energy, field frequency) in which the detail exists are not

necessarily well suited for the determination of spatio-temporal relationships within the global system. The sampling in space is highly detailed but sparse, and very few locations can be sampled simultaneously. Thus, causality is often difficult to determine, and the global significance of any given observation is not necessarily evident.

2. Context: Most observations in magnetospheric physics have no context because of their relative isolation in space and time. Whatever context can be applied is typically rooted in a concept or model of the system accumulated over time by an individual or community of researchers. This lack of definitive context severely inhibits growth of understanding of the system, especially with respect to its global behavior.
3. Intuition: The physical dimensions sampled by the traditional data of magnetospheric physics are not the dimensions of everyday human experience. Therefore, whatever intuition is available to be applied to the study is typically developed at great effort – and not easily shared with an uninitiated lay audience.

A classic example of a study of the use of isolated ion and electron distribution functions to gain understanding of magnetospheric structure is provided by the work of Mauk and Meng (1983). Their painstaking analyses of geosynchronous particle spectrogram shapes led to an understanding of the spatial morphology of energetic particle injections near the inner edge of the plasma sheet. The result is known as the double spiral injection boundary. A single image from a medium energy ENA camera could be sufficient to elucidate such a feature by providing direct visualization of the shape of the energetic ion injection boundary. A series of images from such an instrument will provide direct observation of the dynamics and evolution of these boundaries. Such observations have thus far been unavailable, owing to technological constraints. With IMAGE, we have the first concerted effort to overcome these constraints.

Figure 1, reproduced from Williams et al. (1992), provides an excellent summary of the fundamental aspects of ENA images, the magnetospheric structures of interest in such images, and a representation of an image expected from a high performance (1 deg resolution) ENA camera.

The MENA imager is very well suited to make lower energy ring current observations. The Earth's ring current is characterized by large fluxes of ions in the energy range accessible to both the MENA and High Energy Neutral Atom (HENA) (Mitchell et al., 2000) imagers. As illustrated in Figure 1, these energetic ions are subject to charge exchange collisions with low energy atoms that make up the neutral hydrogen geocorona. These collisions transform the energetic ions into ENAs that exit the interaction region on energetic ballistic trajectories. Thus, the ring current continuously emits ENAs detectable by a properly designed and deployed ENA imager.

The ring current is highly dynamic, undergoing growth and decay as geomagnetic storms wax and wane in response to external (solar wind) driving forces.

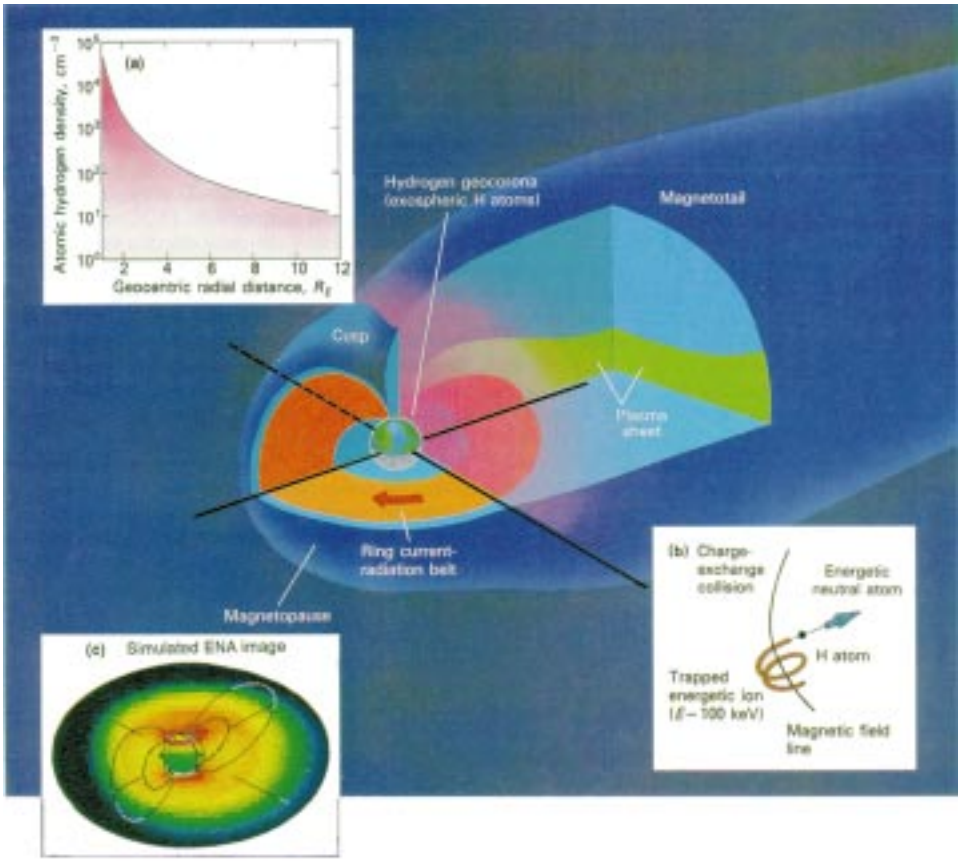

Figure 1. Schematic diagram of Earth's magnetosphere and processes relevant to energetic neutral atom imaging. Insets show: (a) the density profile of the geocorona; (b) a schematic view of collisional charge exchange, the mechanism responsible for ENA creation; (c) a simulated ENA image from a hypothetical imager with 1 deg resolution (from Williams et al., 1992).

Using the MENA imager, we will track injection fronts (Moore et al., 1981) as they move earthward, and correlate their geometry and motion with solar wind and interplanetary magnetic fields (IMF) conditions. We will directly observe the differential drift of ions around the Earth, under the influence of energy-dependent gradient and curvature drift. Global estimates of the ring current decay rate will be provided by combining MENA and HENA observations of ENA escape with global ring current precipitation measurements from the Far Ultra-Violet imager (Mende et al., 2000). Other potential targets of interest for the MENA imager include the near-Earth plasma sheet and the cusp.

1.2. IMAGE MEASUREMENT OBJECTIVES AND THE ROLE OF THE MENA IMAGER

The broad objective of the IMAGE mission is to answer the question: How does the magnetosphere respond globally to the changing conditions in the solar wind? We address this broad objective by posing several more specific questions and designing our instrumentation to provide answers to them:

1. What are the dominant mechanisms for injecting plasma into the magnetosphere on substorm and magnetic storm time scales?
   Solar wind protons with speeds of 500 km s^{-1} possess 1.5 keV directed kinetic energy when they encounter the Earth's bow shock. Higher solar wind speeds are not uncommon. Shocked solar wind plasma is the primary constituent of the magnetosheath, which must be the dominant solar wind plasma source for the magnetosphere. This plasma engulfs the exterior of the magnetopause. At the cusps it has direct access to the ionosphere and thermosphere. The magnetosheath plasma therefore acts both as a source of energy for day side ionospheric outflow and as a source of plasma for the magnetosphere. Particularly during times of large solar wind speed, MENA will be able to image the cusp in few keV magnetosheath protons. The Low Energy Neutral Atom (LENA) imager (Moore et al., 2000), which operates at lower energy than MENA, will make images of the ionospheric outflow on the day side, for comparison to cusp images obtained using MENA magnetosheath observations.
2. What is the directly driven response of the magnetosphere to changes in the solar wind?
   MENA images of magnetospheric regions will show the global magnetosphere response to solar wind changes measured upstream. Time series of global magnetospheric properties will be directly compared with time series of solar wind and interplanetary magnetic field conditions.
3. How and where are magnetospheric plasmas energized, transported, and subsequently lost during storms and substorms?
   Within the magnetosphere, substorm and storm-time plasma injections will be imaged using MENA. Near-Earth plasma sheet and energetic plasma injections in the tail will be primary observational targets. The shape of injection boundaries in space will be visualized. If these boundaries propagate, we will observe their global propagation, measure propagation speeds, and track the evolution of the boundaries and their plasma populations. The variation in energy of the injected particles as a function of time and position will be measured using MENA. The plasma sheet tailward of injections may be imaged on longer time scales. The MENA imager will be in an excellent position to view the plasma sheet (kT $\sim$10 keV) and its extensions to low altitudes in the nightside auroral zones. The global evolution of the plasma sheet before and after tail unloading is directly connected to the injection mechanisms themselves.

The transport of energetic ring current particles subsequent to injection will be revealed using time series of ring current images. Resultant energy and mass distribution and loss will be parameterized and tracked using MENA observations.

The MENA imager is intended to operate in concert with the other instruments on IMAGE to answer the above questions. It is well suited to address each, using ring current, magnetosheath, and plasma sheet observations, as discussed above.

1.3. Instrument Requirements, Performance, and Resources

In order to achieve the scientific objectives described above, the MENA imager is required to provide ENA flux images of hydrogen and oxygen. The images are required to be provided with 8-deg angular resolution, 80% energy resolution, and 2-min time resolution over the energy range from 1 keV to 30 keV for the 2-year duration of the prime mission.

All of these requirements are fundamentally met by the flight instrument, and generally the imager performs very well. However, the performance across the entire instrument sample space does not uniformly meet these requirements. For example, heavy ENAs scatter in the foil to large angles at low energies, irreducibly limiting the angular resolution of downstream optics and detectors (see Figure 10). Thus, 8-deg angular resolution is not achieved for oxygen within the MENA energy range, as it is for hydrogen and helium. However, the imager energy range extends to 50 keV and above (limited by the short end of TOF). Furthermore, this angle measurement deficiency exists only in the polar (imaging) angle. The azimuth (spin phase; collimated) angle is not affected. A second example of the instrument's inability to fully satisfy the performance requirements involves species determination. This topic is discussed below and in Section 3.4.

The more energetic (30–50 keV) oxygen will be imaged with full resolution by MENA. Specified polar angle resolution is achieved for hydrogen at energies slightly greater than 3 keV. MENA will do an excellent job measuring polar incidence angle of ring current and plasma sheet hydrogen and oxygen at energies above those called out directly above, but not below those energies. The energetic tail of Earth's magnetosheath ions will be nicely imaged by MENA. Charge exchange targets will be sparse, however, except during periods of extremely high solar wind ram pressure, when the magnetopause will be forced to small geocentric locations. The mid-altitude cusp should be very nicely and simply imaged in its high-energy hydrogen tail using MENA.

The MENA imager concept was selected from among several promising ideas that have been put forward during the last five to ten years (McComas et al., 1991, 1994, 1998; Gruntman, 1997). The slit camera concept (McComas et al., 1998) was selected due primarily to the very large (approximately 24 cm^2) aperture presented to space.

TABLE I
MENA required and achieved performance

Quantity	Requirement	Performance (O)	Performance (H)	Units
Angle FOV				
Azimuthal	360	360	360	degrees
Polar	90	140	140	degrees
Angle resolution				
Azimuthal	8	5	5	degrees
Polar	8	12	8	degrees
Energy range	1–30	3–70	1–70	keV
Energy resolution	80	80	80	%
Species ID	H, O	probabilistic	probabilistic	unitless
Effective area*	1.0	0.83	0.83	cm^2

*3 sensors combined.

TABLE II
Physical resources for the MENA Imager.

Quantity	Value	Units
Mass	13.9	kg
Power	22.5	W
Data Rate	4.3	kbps
Dimensions	42.5 × 22.3 × 29.3	cm × cm × cm

The weakest aspect of the MENA slit camera approach is that only the speed is directly measured, using time of flight. Energy per charge is not independently measured and therefore mass per charge is not directly derivable from the data in this way. Using the slit camera approach as in the case of MENA, species may be inferred with finite certainty as described in Section 3.4. These limitations were known at the time of the selection of the MENA instrument concept. For a first ENA instrument in this energy range, we prioritized larger geometric factor and simplicity over certainty with respect to mass.

Table I lists the performance requirements described above, as well as measurements and estimates of the performance achieved by the flight MENA imager. Details are to be found in the text of this paper and in direct consultation with MENA team members.

Table II lists a number of critical physical parameters and spacecraft resource requirements associated with the MENA imager as delivered for flight.

2. MENA Measurement Approach and Implementation

2.1. OBJECTIVES VERSUS CONSTRAINTS

The unique challenges in developing a medium-energy ENA imager lie in the nature of the species under study and the environment in which the imager operates (Gruntman, 1997). Unlike charged particles, ENAs are not responsive to electric or magnetic fields, and therefore they cannot be steered through an electrostatic or magnetic analyzer. Unlike photons, ENAs do not pass through solid lenses or specularly reflect at large angles off of polished surfaces (grazing incidence specular reflection, with ionization, of low-energy ENAs is used in LENA imager (Moore et al. 2000)). Medium-energy ENAs can therefore not be steered through conventional reflective or refractive optical systems. Finally, unlike the most energetic ENAs, those in the energy range 1–30 keV are not energetic enough to (a) generate measurable charge in a solid state detector or (b) pass through a relatively thick (a few μg cm^{-2}) UV rejecting foil (not to be confused with UV blocking gratings) without severe scattering and attenuation.

The MENA operational environment is distinguished foremost by the presence of intense fluxes of UV photons, primarily hydrogen Ly-α, of both solar origin ($\sim 5 \times 10^{11}$ cm^{-2} s^{-1}) (Hall et al., 1985) and from the Earth's day glow ($\sim 4 \times 10^{9}$ cm^{-2} sr^{-1} s^{-1}) (Meier, 1991). This flux is a potentially crippling source of background noise, which is particularly troublesome in view of the low fluxes of medium energy ENAs to be measured. The MENA imager approach described here has been developed to address these issues and provide the largest possible scientific return.

2.2. TOF/SLIT CAMERA APPROACH

By analogy to the canonical pinhole camera, MENA uses the wide-slit camera approach to ENA imaging as first suggested by McComas et al. (1998). The concept is schematically illustrated in Figure 2. A slit camera is distinguished from a pinhole camera in that it provides only 1D imaging (transverse to the slit), whereas the pinhole camera provides fully 2D imaging. In the MENA case, the second image dimension is acquired using collimation and spacecraft spin.

The ENA polar angle is determined based on knowledge of two-dimensional (2D) position at two points along the incident trajectory. The simplest implementation is a very narrow slit, in which the first trajectory location is known a priori. However, we have implemented a wide slit to increase the aperture area, and therefore sensitivity, due to the low ENA fluxes. The added sensitivity comes at the price of added complexity. In the wide-slit case of the MENA imager, the incident ENA position within the slit must be determined independently (McComas et al., 1998). This position and the position of the second trajectory point (fixed at the detector plane) are independently determined using a single segmented position-sensitive detector.

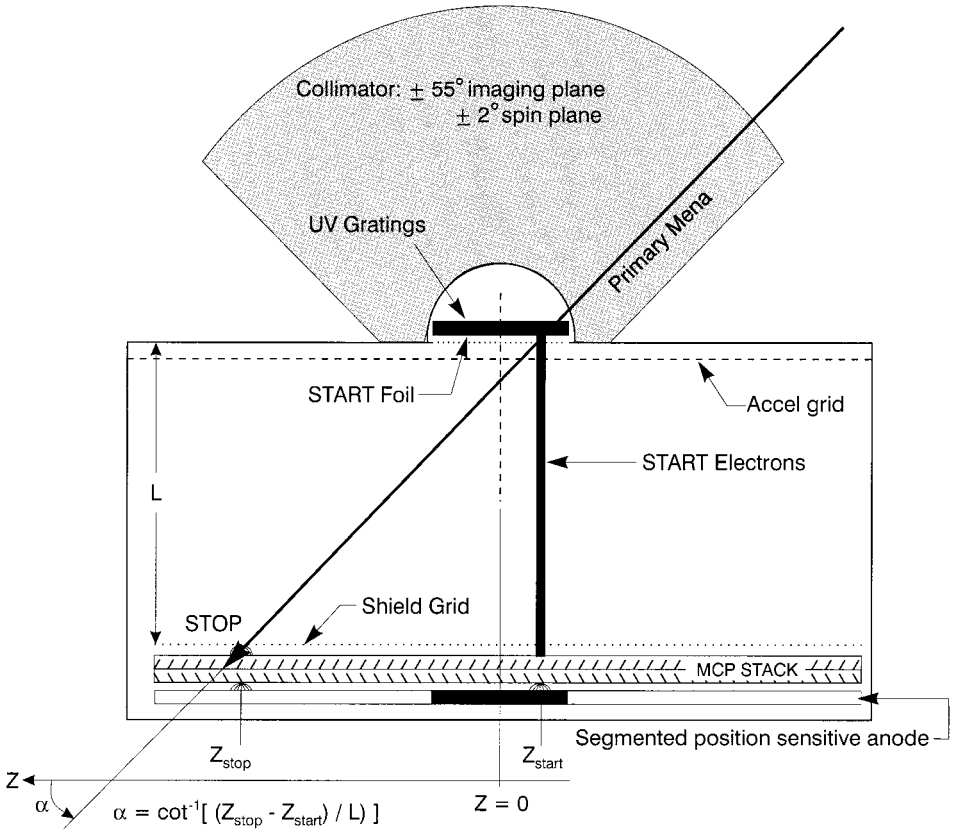

Figure 2. Schematic view of a MENA sensor. A neutral atom passes through the START foil, producing secondary electrons. Secondary electrons are accelerated towards the START segment of the detector, whereas the ENA will impact the detector STOP segment. Particles incident on the START and STOP segment of the detector will provide TOF timing signals, which together with their respective pulse height and ID position on the detector provide the required information for polar incidence angle, energy and species determination of the ENA.

3. Instrument Description

3.1. Overview

A functional block diagram of the MENA imager system is provided in Figure 3. An isometric drawing of the imager and photograph taken just prior to calibration are presented in Figures 4 and 5, respectively. The MENA imager is composed of three identical sensors, labelled as shown in Figure 4 and mounted to a common DPU assembly. Each sensor is supported by two dedicated front-end electronics (FEE) cards (time of flight, or FEETOF, and pulse height analyzer, or FEEPHA) and a triple function (+10 kV, +4 kV, −1 kV) high-voltage power supply (HVPS). The three sensors share common low-voltage power sources (LVPS), high-voltage

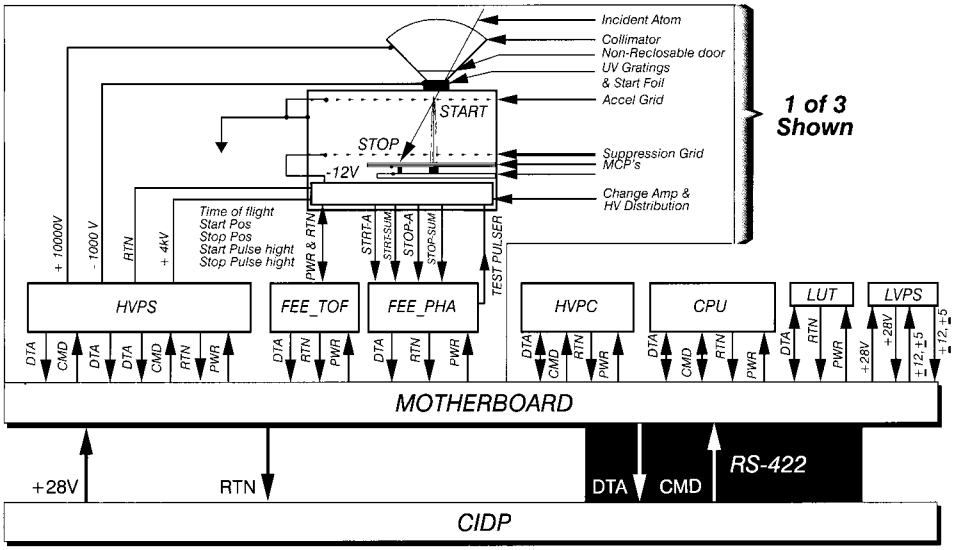

Figure 3. MENA Imager block diagram. All electrical interfaces to the spacecraft, other than chassis ground, are those shown to the CIDP. Only one of the three identical sensors, HVPS, FEE, TOF, and FEE_PHA subsystems are shown, though they are indicated to be three.

and pulser control circuitry (HVPC), data acquisition, lookup table, and storage facilities (MLUT), and a microcontroller (CPU) for command and data processing and interface to the IMAGE Central Instrument Data Processor (CIDP) (Gibson et al., 2000). The three sensors each provide 1D imaging of incident ENAs in the polar angle direction based on a spherical coordinate system defined using the spacecraft positive spin axis as the $+z$-axis. The second imaging dimension (azimuth) is obtained using collimation and spacecraft spin. The sensors are mounted to provide look directions that view a common azimuth (spin) angle, but are offset from one another in their polar angle field of view. The center of the Sensor 2 look direction is perpendicular to the spin axis, at a polar angle of 90 deg. The centers of the Sensor 1 and 3 look directions lie at polar angles of 110 deg and 70 deg, respectively. Each sensor has a 20-deg wide blind spot associated with the Start anode segment in the center of its field of view. The 20-deg offset among the sensors was selected to eliminate the blind spots and produce a constant instrument response when the three sensors are combined. The spacecraft coordinate system is also shown in Figure 4, for reference.

ENAs, charged particles, and photons incident from within a sensor's field of view enter through the collimator, where charged particles with energies up to 13 times the adjustable applied voltage are removed by electrostatic deflection. The remaining particles and photons must pass through a free-standing UV blocking grating, where the UV photons are removed around a very wide stop band by the optical properties of the grating. The grating structure was designed to eliminate the 121.6 nm (solar hydrogen Ly-α) light reflected from the geocorona. Within the

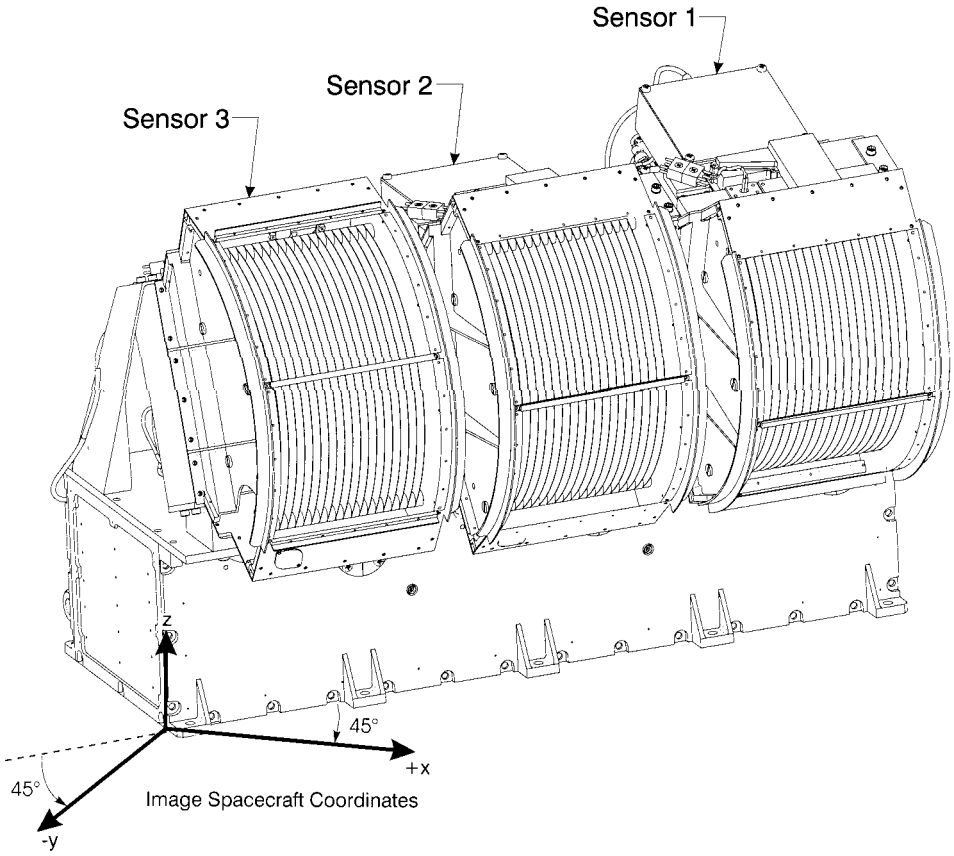

Figure 4. Isometric drawing of the MENA imager. Shown are the three identical MENA sensors, mounted on the DPU unit. The detectors are offset 20 deg in the azimuth (spin) angle direction. The spacecraft coordinate system is also shown, for reference. Compare with Figure 2, where we have shown the coordinate system applicable to each of the three sensors.

aperture, the ENAs pass through a thin carbon foil where they produce secondary electrons and undergo angular scattering that depends upon the species and energy. Secondary electrons are accelerated to the MCP detector Start segment, while the primary ENA continues along its trajectory to impact the MCP detector Stop segment. ENAs incident on the stop detector segment and their correlated secondary electrons incident on the Start detector segment provide position measurements from which the ENA polar angle is calculated. This information is combined with TOF timing signals to yield a determination of speed. Detector pulse heights are used to provide information on species and detector health. UV photons not absorbed by the UV blocking gratings are not counted due to the TOF coincidence requirement.

Start and Stop MCP pulses stimulate charge-sensitive amplifiers (CHAMPS), housed at the rear of the detectors. CHAMP outputs are fed through lower-level

discriminators (LLD, located in the DPU) to the FEE where they are analyzed for charge magnitude, relative timing, 1D ratiometric position, and conformance to specified logical valid event criteria. For a valid event, the result of this analysis is 5 bytes of data that, along with spin phase and sensor identification, comprise the core raw data associated with a detected ENA. These data are provided to the Mass Look-up Table (MLUT), which uses them to form images in hardware memory. These hardware images are accessible to the Central Processing Unit (CPU) for selection or collapse, followed by formation into data packets for telemetry downlink. The MLUT, residing in EEPROM, is populated with data that embody knowledge of the imager response, in principle making is possible for the raw data to be interpreted in terms of ENA incidence angle, energy, and species. Image data products formed using the MLUT, as well as other data products described below, are packetized and delivered to the Central Instrument Data Processor (CIDP) (Gibson et al., 2000) for optional compression and telemetry downlink.

Flight electrical interfaces to the IMAGE spacecraft include +28 V instrument bus power (from which all routine functional power is derived), +28 V heater bus power, which is used only to open each sensor's non-reclosable door; and a bi-directional RS-422 interface to the CIDP. All command and telemetry data pass through the RS-422 interface. Further details of the DPU are provided in Appendix A.

3.2. SENSOR OPTICS

The MENA imager is composed of three identical sensors, numbered as in Figure 4. The sensor design concept is illustrated in Figure 2. Each has a collimator, an aperture populated with UV blocking gratings and thin carbon foils, a grounded acceleration grid, a field-free drift chamber, and a segmented 1D position-sensitive detector.

Incoming ENAs, charged particles, and photons must pass first through an 85%-transmission grounded screen placed on the front face of the collimator and then through the collimator itself. The vanes on the collimator are blackened with a dendritic cupric oxide (Ebanol-C) to absorb photons and charged particles, and arranged geometrically to allow a nominal 4 deg FWHM azimuthal resolution. This angular band pass is aligned at a constant spacecraft azimuth angle. Alternate vanes are grounded or electrically biased at up to +10 kV (determined by ground command) to sweep out charged particles with energies per charge up to approximately thirteen times the applied bias voltage. Laboratory measurements show charged particle transmission at 30 keV to be 10^{-4}, with 5 kV applied to the collimator vanes.

Those ENAs and photons that are transmitted though the collimator impinge upon the aperture, which is rectangular in shape and approximately 8 cm × 1 cm in area (the 1 cm dimension is imaged while the 8 cm dimension is not). The aperture is populated with five rectangular assemblies, each comprising one free-standing

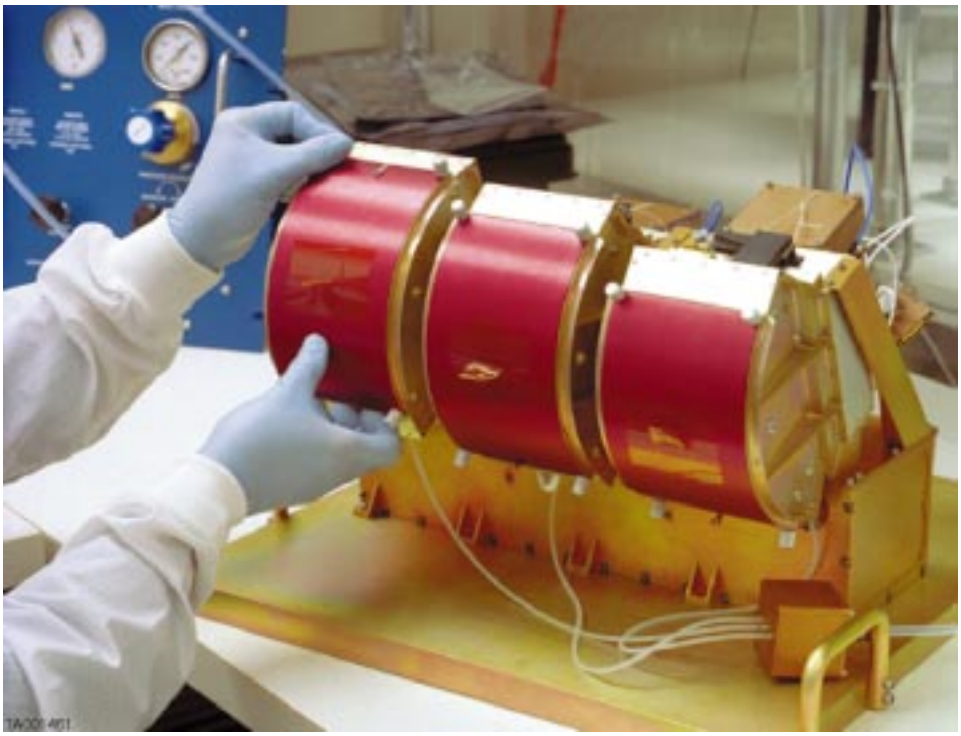

Figure 5. Photograph of MENA imager prior to calibration. The large handling base plate with handles, protective red covers, and purge distribution system (small alodyne coated box with purge lines in and out) are all non-flight.

gold UV blocking grating and a thin carbon foil. Each grating/foil assembly has a 1.6 cm $\times$ 1.0 cm rectangular shape. The purpose of the gratings is to pass ENAs while blocking UV photons. They were developed and manufactured for the MENA imager at the Massachusetts Institute of Technology (MIT) using holographic lithography techniques (Van Beek et al., 1998). A schematic diagram of the grating structure is shown in Figure 6.

The grating consists of an ensemble of gold bars, each with a thickness of 400 nm and a width of 160 nm. The bars lie parallel to one another with a periodic spacing of 200 nm. A critical parameter for the absorption of hydrogen Ly-α is the $\sim$40 nm spacing between the gold bars. The gold bars are supported on nickel grids, much coarser and stronger than the gold gratings themselves. The Ni grids provide a strong substructure on which to support the gold without severely reducing geometric open area of the grating. The gold grating ensemble acts as both as a strong polarizer and a lossy wave guide, tuned for maximal absorption of hydrogen Ly-α ($\lambda = 121.6$ nm) photons, the dominant source of UV noise in near-Earth space. Photons at shorter and longer wavelengths have higher transmissions

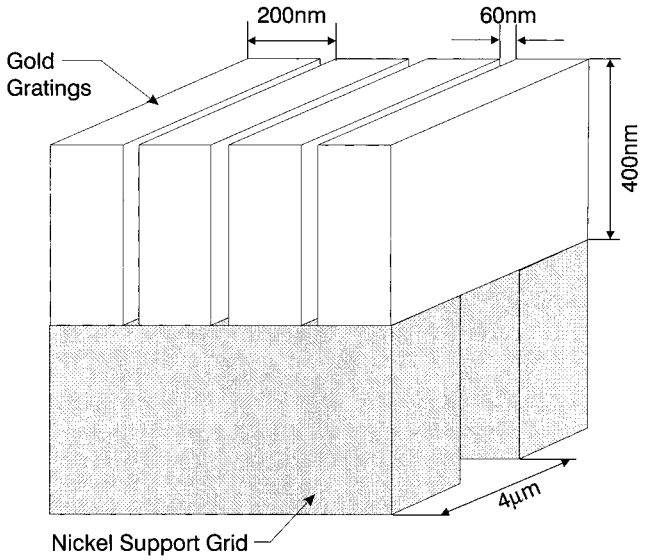

Figure 6. Schematic diagram of UV transmission gratings. The drawing is not to scale. Therefore, disparate dimensions like the 60 nm gaps between gold bars and the 4 μm nickel grid period are displayed on similar scales.

than hydrogen Ly-α, but hydrogen Ly-α fluxes are by far the dominant source of UV noise near Earth.

The photon transmission of prototype gold gratings has been modeled as a function of wavelength and measured in the laboratory (Gruntman et al., 1995; Scime et al., 1995; Balkey et al., 1998). The results are shown in Figure 7. The solid curve is the model result, and the data points are measurements. Figure 7 shows that the transmission of the prototype gratings at 121.6 nm is $\sim 3 \times 10^{-5}$, while that at 30.4 nm and 58.4 nm is 5×10^{-2} and 1×10^{-2}, respectively. These measurements serve as spot checks on the model; both show good agreement. This result gives confidence that the expected grating performance will be attained in flight. The flight gratings differ slightly from the prototypes whose performance is shown in Figure 7. MENA flight gratings also have been modelled and measured. They show uniformly superior UV attenuation to that shown in Figure 7.

The flight grating photon transmission has been convolved, as a function of wavelength, with the geocoronal emission profile of Meier (1991) to estimate the total noise rate in a MENA sensor due to geocoronal luminescence. The result, shown in Figure 8, shows both the differential (with respect to wavelength) and total (integrated over wavelength) MCP count rate near apogee due to geocoronal photons. The total expected noise rate is shown to be less 250 Hz, yielding a predicted (accidental) coincidence rate of only a few mHz due to the UV background.

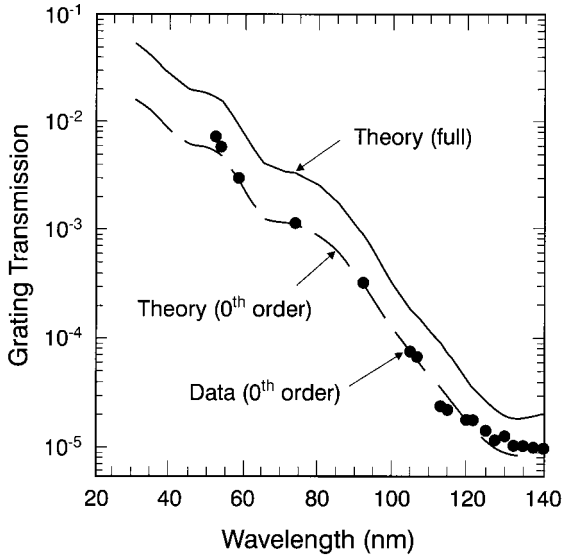

Figure 7. Model and measured photon transmission through MENA prototype gratings. The solid curve represents model results, points indicate measurements.

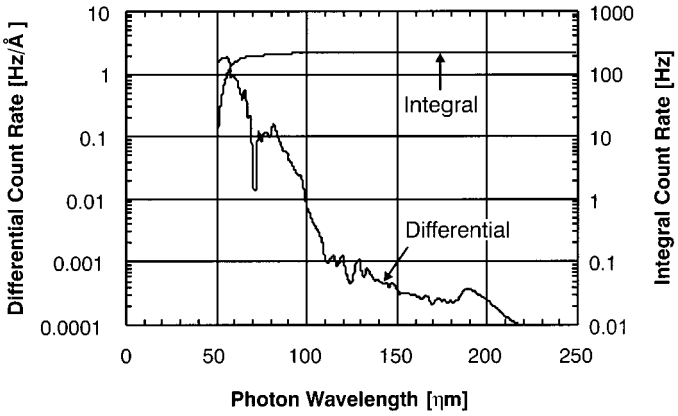

Figure 8. Background noise rate due to geocoronal photons. Shown are the total (STARTS + STOPS) expected MCP count rates due to UV photons near the IMAGE apogee. Both differential count rates and their integral are shown and labeled.

Figure 9 shows measurements of the particle transmission plotted versus hydrogen Ly-α transmission for the fifteen gratings installed in the flight MENA imager. The data points are labelled according to whether the gratings were installed in Sensor 1, 2, or 3. The hydrogen Ly-α transmission for these samples ranges from 6×10^{-7} to 2×10^{-5}, with a mean value of 6×10^{-6}. The particle transmission ranges from 4.1% to 7.8%, with a mean of 5.1%. Taking the sensitivity of microchannel plates to be 0.8 and 0.01, for ENAs and hydrogen Ly-α photons, respectively,

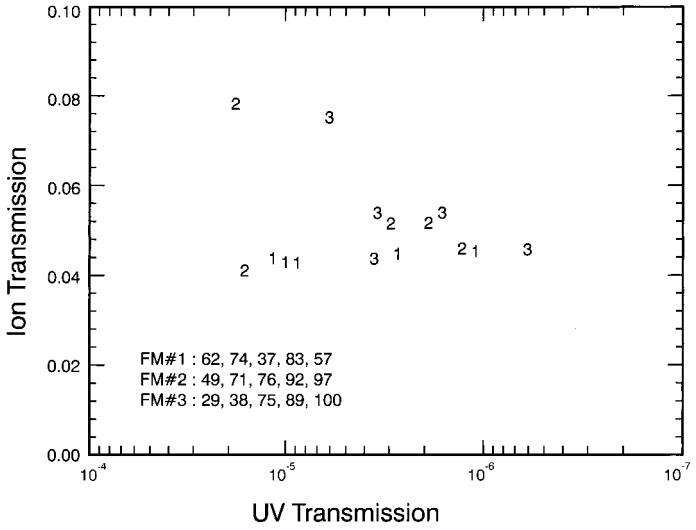

Figure 9. Particle and UV transmission map for MENA flight gratings. Data points are labeled with the number of the sensor in which they were installed. Individual serial numbers are tabulated, also according to sensor.

the MENA sensitivity for ENAs is seen to be larger than that for hydrogen Ly-α photons by a factor of 7×10^5!

ENAs that pass through the gold grating impact a thin (nominally 0.6 or 0.7 μg cm^{-2} for MENA flight foils) carbon foil that has been affixed to the back face of the grating. In the past, carbon foils have been floated onto metal grids that were clamped into grid holders. We chose to float the foils directly onto the gratings and avoid a 35% ENA transmission deficit associated with the metal grid. The purpose of the foil is to generate secondary electrons due to the interaction of the ENA with the carbon foil. The secondary electrons mark the z-coordinate of the ENA as it passes through the aperture (see Figure 2) and produce a Start signal for the TOF system. The number of secondary electrons emitted provides information regarding the ENA species. Emission of secondary electrons from the foil is a probabilistic phenomenon and can only be quantified in statistical terms. The energy of the emitted electrons is broadly distributed near a few eV. Their angular distribution is peaked about the forward direction. Both emission angle and energy are largely independent of the characteristics of the incoming ENA. The secondary electron yield (number of electrons emitted per incident ENA) is also a probabilistic quantity that is influenced by the mass, speed, and incidence angle of the ENA. At energies less than a few hundred keV, the yield increases for ENAs that are faster, heavier, and incident at larger angles with respect to the foil surface normal.

The entire assembly for each sensor is cosists of five carbon foils, gold gratings, and stainless steel grating frames. It is clamped into a light-tight mounting assem-

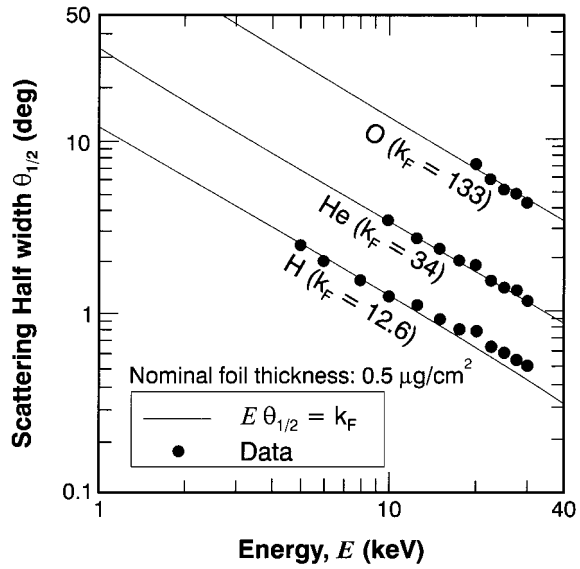

Figure 10. Angular scattering of ENAs upon passage through nominal a 0.5 μg cm^{-2} foil (from Funsten et al. (1993)).

bly in the sensor aperture and electrically biased to -1 kV with respect to chassis ground. Since the secondary electrons are emitted with a broad angular distribution and energies of a few eV, the -1 kV bias is required to accelerate electrons toward the detector, thereby retaining the z-coordinate of the ENA passage through the aperture. A grounded (85% transmission) grid is placed 1 mm downstream from the carbon foil, inside the sensor. Secondary electrons are accelerated to 1 keV through this grid and pass through a nearly field free 3 cm (L in Figure 2) region before striking the detector over the Start anode segment. Thus, they provide the TOF Start signal and the z-coordinate of detector impact, which is interpreted as the z-coordinate of ENA passage through the aperture, or Start position. The pulse height of the MCP charge burst, or Start Height, is measured and recorded to assist in the statistical measurement of PHA for species identification.

ENAs undergo energy- and mass-dependent scattering during passage through the foil, causing some degradation in our ability to measure polar angle for incident ENAs. Figure 10 contains results of a laboratory study by Funsten et al. (1993), applicable to ENA scattering in a nominal 0.5 μg cm^{-2} foil These data may be interpreted directly as a lower bound on the scattering half angle for ENAs passing through the MENA aperture, and therefore as a lower bound on the (half width) polar angle resolution achievable using the MENA imager. The angular resolution in the collimated azimuth direction is not affected since the collimator fixes this at approximately 5 deg FWHM.

An incoming ENA continues (nearly) along its original trajectory and strikes the detector over the Stop anode segment, providing the TOF Stop signal, the z-

coordinate of ENA impact on the detector (or Stop Position), and the pulse height of the Stop MCP charge burst, or Stop Height. Like the Start Height, Stop Height is related to ENA species. The path length of the ENA from the aperture to the detector is $(3/\cos(\alpha))$ cm, where α is the measured polar incidence angle as shown in Figure 2. The timing of the Start and Stop signals is compared in the FEETOF to produce a time of flight.

In view of the -1 kV accelerating potential applied to the carbon foil, a secondary electron's transit time from foil to detector is $\sim$1.6 ns, assuming initial secondary electron energy of 2 eV and a 45-deg emission angle. During this time, an electron will have travelled less than 1 mm transverse to the aperture normal (z-direction). This displacement adds to the uncertainty in the measurement of the z-coordinate of the ENA as it passes through the aperture, and therefore, in the ENA polar angle which is derived from it. The choice of -1 kV acceleration potential represents a compromise between the requirement to minimize the electron's transverse displacement, on one hand, and the distortion of the ENA trajectory after passage through the foil, on the other hand. The latter is a consideration because of the fact that a significant percentage of ENAs will emerge from the foil with a non-zero charge state and will be subject to trajectory distortion in the applied electric field.

3.3. DETECTOR SYSTEM

The detector system fastens into the back of the sensor as a sub-assembly. It is composed of a z-stack MCP array, a segmented 1D position sensitive anode with independent Start and Stop regions, four CHAMPS (Start A&B, Stop A&B), and a network of resistors and capacitors to distribute high voltage and filter out noise.

The detector is based on large area rectangular MCPs, similar to Hamamatsu commercial model 2396-04, but manufactured specially for the MENA imager according to provided specifications. The MCPs provide large area (72 mm $\times$ 90 mm), relatively high resistance ($\sim$100 M-Ohm per plate), high gain due to channels with 60:1 length-to-diameter ratio, and narrow pulse height distribution (as low as 70% over the entire detector). They also operate with low noise ($<$1 cm^{-2} s^{-1}), very low rate of after-pulsing as required for the TOF work, and excellent uniformity ($<$10% variations over their surface).

Representations of the front face (MCP side) and rear face (connected to CHAMPs) of the anode are shown in Figures 11(a) and 11(b). In Figure 11, we present the actual anode layout drawings, modified for this illustration. Importantly, alternate bars have been removed for this illustration (front and rear) for the sake of clarity. The small pads shown are sites for mounting surface mount resistors, as called in the detail, Figure 11(a). On the top side (Figure 11(a)), one MΩ resistors are used in these locations. On the bottom side, small (100 Ω) resistors were used during early development, but the MENA imager was calibrated and will fly with 0 Ω (short circuit) resistors in place.

The anode performs several functions. First, it decouples the detector high voltage such that the front face operates at positive high voltage and the back face operates at ground. MCP charge bursts are capacitively coupled to the back side through the alumina substrate. Second, it isolates and separately processes Start and Stop events from the detector, using separate charge amplifier pickups for Starts and Stops. These are shielded from one another by grounded 'gutters' that necessarily act as dead spots on the anode. Third, the anode provides 1D position encoding using capacitive charge division independently for Start and Stop anode segments. Note that, although the two Stop segments to the left and right of the central Start region are physically separated on the substrate, the two portions of the A side and the two portions of the B side are electrically connected at the inputs to the Stop A&B CHAMPs. Electrically, they form contiguous A and B Stop anode segments.

The 1D position encoding anode functions as follows: Charge deposited by the MCP will land on one or two of the conducting bars of the uniform array on the front face of the anode. The charge will promptly distribute itself uniformly along the length of the bar and reside there for a period of time until it bleeds off through the terminating resistor. The bar capacitively couples to the back face of the anode, more or less strongly to the A- or B-side depending on the capacitance. This coupling will drive electrons off backside conductors and onto the inputs of the respective CHAMPs. Stronger capacitive coupling to the A- or B-conductor array results in proportionally more charge being driven onto the attached CHAMP. Note the opposing linear variation in the lengths of the A- and B-conductors with z. The ratio of charge delivered to the A- or B-CHAMP to that delivered to the A- and B-CHAMPs (equal to total deposited by MCP) is itself a linear function of z. This ratio is encoded by the FEEPHA card and calibrated with respect to position.

The detector is serviced by four (Start A&B, Stop A&B) CHAMPs. Each is a fast charge-sensitive amplifier that integrates charge deposited on its input and creates a bipolar output pulse. The CHAMPs are designed to provide a uniform time interval from charge deposition to the zero-cross at transition from positive to negative lobe. They are tuned to provide gains of 0.15 V/pC. The CHAMPs' output stages are wired such that the four outputs provided to the FEE are StartA, StartSum, StopA, and StopSum. StartSum and StopSum are the sum of the A- and B-signals for Start and Stop pulses described in the above paragraph.

3.4. EVENT PROCESSING

The four CHAMP outputs listed above represent the complete response of a sensor to a detected ENA. These signals are provided to the FEE for analysis and valid event determination. The response of the FEE to CHAMP outputs depends on their characteristics. The minimum response for StartSum or StopSum pulses which exceed commandable LLD thresholds is to increment Start and Stop counters that are read out and reset 45 times per spin as part of the StartStops data product. In the

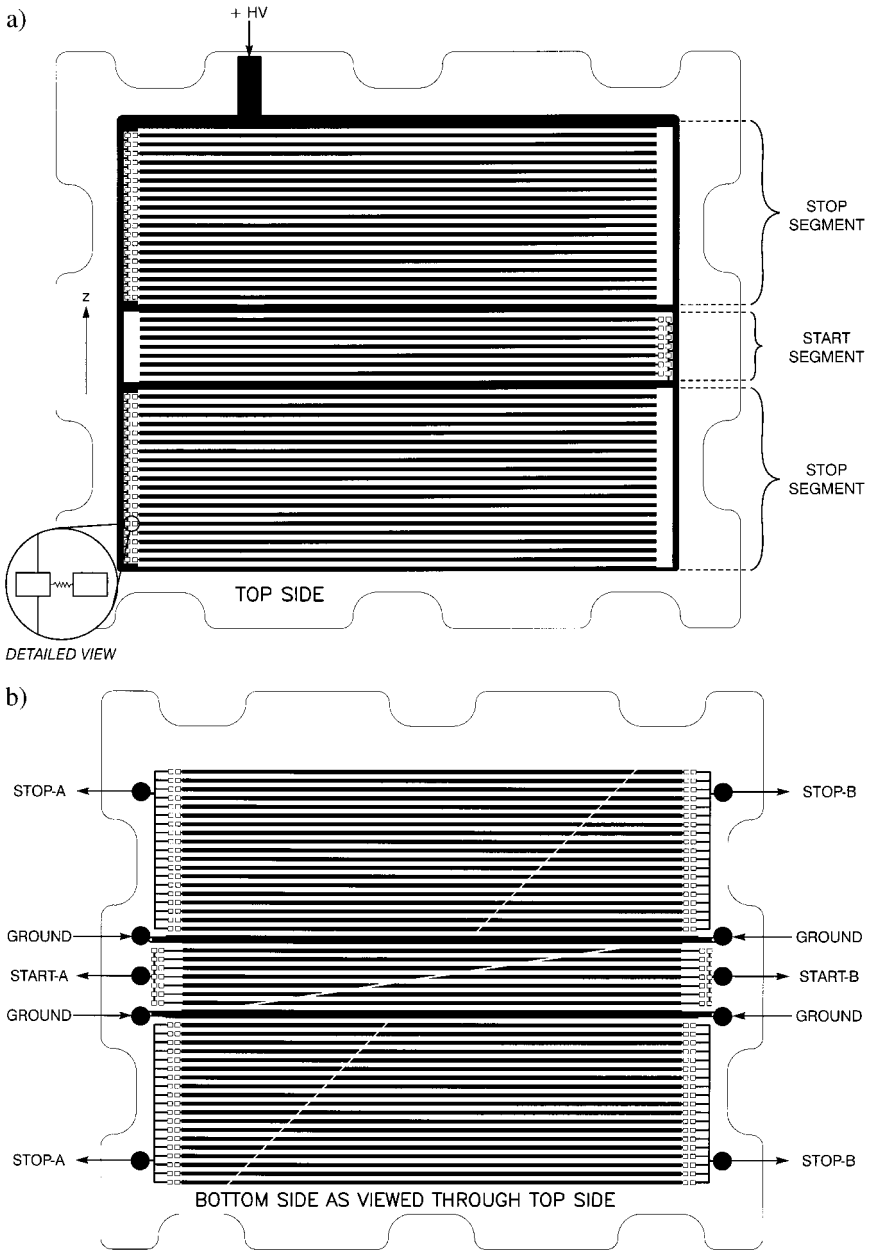

Figure 11. Schematic representation of the MENA front (a) and rear (b) anode surfaces. Start and Stop anode segments are indicated, as is the shape of the alumina substrate. The black regions in both diagrams show gold-coated copper conductors. Every other conducting bar has been removed for this illustration for clarity. The detail in (a) shows that surface mount electrical resistors are installed on the small pads near the end of signal pick-up bars. The z (imaging) direction is marked in (a). (b) is shown as if one could view the bottom side through the top side of the anode.

case of a StopSum pulse not immediately preceded by a StartSum pulse, the FEE responds no further. In the case of a StartSum pulse, the FEE decides whether a Valid Event has occurred. If no Valid Event is declared, the FEE increments one of 10 Singles counters corresponding to an identified error condition (StartStop and Singles data products are described more fully in Section 5). If a Valid Event is declared, the FEE increments a Valid Event counter which is read out and reset 45 times per spin, completing the StartStops data product. In this case, the FEE also reports five bytes of data to the MLUT. These include Start Position, Start (pulse) Height, Stop Position, Stop (pulse) Height, and Time of Flight.

With respect to Figure 2, the incident polar angle (α) and speed (s) of a detected ENA are determined from the FEE data as

$$\alpha = \cot^{-1}[(Z_p - Z_t)/L] \tag{1}$$

and

$$s = 3.0/(t\ \sin(\alpha))\ . \tag{2}$$

Here α is the polar angle shown in Figure 2, z_p and z_t are Stop and Start positions in cm, L is the distance between the foil and the MCP (also in cm), t is the time of flight in seconds, and s is the ENA speed in cm s^{-1}. It is noted that z_p, z_t, and t are related to corresponding bytes delivered by the FEE in a fashion that is ideally linear but in reality will only be approximately linear. Specification of the true relationship between the physical quantities and their byte representation comes from the laboratory calibration.

Determination of ENA species with the MENA imager can only be done in a statistical sense. The approach is to utilize the observed dependence of the secondary electron yield from carbon foils on the speed and mass of incident ENAs to differentiate between species. Larger secondary electron yield at the carbon foil will produce larger Start Heights, and larger yields at the Stop MCP input may yield larger Stop Heights. Therefore, comparing Start and Stop Heights among events with similar speeds provides a basis for species identification. Figure 12 shows data published by Ritzau and Baragiola (1998) that demonstrate increasing secondary yields with increasing primary ENA speed and mass. Owing to the statistical nature of the emission process (approximately Poisson), the width of the yield distribution for a single species at a fixed speed is large enough that the yield distributions for H, He, and O with equal speeds overlap substantially. Thus one can only derive probabilities that individual events are associated with a given ENA species based on the data available from the MENA imager. The MENA Image data (Section 5.1.1) will use the assumption that the species is Hydrogen. The bulk of the data will be sorted by pulse height on the ground, allowing tentative identification of species within bands of pulse height.

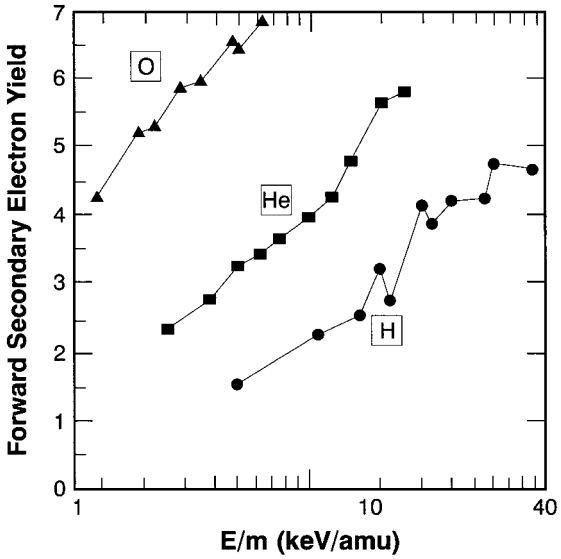

Figure 12. Dependence of the forward secondary electron yield upon ENA speed, showing an increased average yield with both particle mass and speed (from Ritzau and Baragiola, 1998).

4. Operations

4.1. MODES

The MENA imager has three operating modes: Low-Voltage Science, High-Voltage Science, and Engineering. Only the High-Voltage Science mode allows application of high voltages and therefore the detection of ENAs. The Low-Voltage Science mode is identical to the High Voltage Science mode, except that high voltages cannot be applied. The Engineering mode allows execution of a class of commands not allowed in the other modes, such as memory loads and software patches.

4.2. COMMANDING

Although the flight software supports a full suite of ground commands, elective commanding of the MENA imager is expected to be kept to a minimum once stable HV operation is achieved. Occasional adjustment of the detector HV levels and the FEE LLD thresholds throughout the mission are anticipated. Adjustment of the ENA spin segment definition, described below, may be required twice per orbit. The three sensors can operate independently of one another. That is, their high voltage levels and LLD thresholds are independent. If one or more sensor suffers an anomaly or displays performance variations, that sensor can be operated at different voltages or thresholds, or can be shut down altogether, without influencing the operation of the other two sensors.

4.3. DATA ACQUISITION

Two data acquisition cycles are defined for the MENA imager. These operate simultaneously and asynchronously with respect to one another. In one cycle, the spacecraft spin is divided into 45 intervals, each 8 deg in azimuth, that are called StartStop bins. Acquisition and reporting of the StartStop and Statistics data products described below are based on this cycle. In the other cycle, ENA and anti-ENA viewing spin segments are defined based on the portion of the spin for which we do and do not expect ENA fluxes to be detected. Definition of the ENA and anti-ENA portions of the spin may be modified by uplink command. Near apogee, the ENA portion of the image will be Earthward viewing. Near perigee, the ENA portion of the image may be anti-Eathward viewing. Two commands per orbit can implement such a scenario. Error Singles and Image data products (also described below) are based on the ENA/anti-ENA cycle. Error Singles are reported from both ENA and anti-ENA spin portions. The Image data products are only reported from the ENA portion of the spin.

The ENA spin segment is by default defined to be 128 deg wide and centered on local nadir. This definition may be adjusted by ground command. The definition of the ENA spin segment may be modified, for example, to view more tailward in the dawn/dusk orbital configuration, or to place the ENA spin segment in such a way that facilitates 'inside-out' viewing as appropriate for observing at low altitudes.

4.4. SUN SAFING

The aperture UV gratings provide sufficient hydrogen Ly-α extinction to allow science observations when viewing toward the Earth, but will not prevent large MCP count rates whenever the Sun is within the MENA field of view. Though the rates from viewing the Sun are not expected to be large enough to damage the MCPs on a short time scale, they may be large enough to reduce their lifetime. Therefore autonomous Sun safing is executed on orbit. Two algorithms are used. Periodic Sun safing reduces the MCP voltages every spin as the Sun spins through the MENA field of view and then returns them to their nominal values. This action is based on a Sun pulse received from the CIDP (Gibson et al., 2000). The angular width and depth of the period of reduced MCP voltages may be adjusted by ground command. Emergency Sun safing is performed through on-board monitoring of Start and Stop count rates. If either of these rates for any sensor exceeds a threshold value more than a specified consecutive number of times, then the high voltage for that sensor will be shut off and a flag will be set for reporting in telemetry. This condition will require intervention by ground operators to return that sensor to normal operation. The counting thresholds and number of exceedences allowed may be modified by ground command.

5. Data Products

Four data product levels are produced. Level 0 data is the raw telemetry data. Level 0 data is not distributed, but is instead used to derive Level 0.5 data, which is archived at the National Space Science Center (NSSDC). Level 0.5 data consists of the entire imager Level 0 data set, together with ancillary data such as calibration factors and standard facilities for converting the raw data to physical units and for retrieval and display. Level 0.5 data is stored and distributed on physical media in Universal Data Format, described by Gurgiolo (2000). Level 0.5 data will form the primary working set for scientific and engineering analysis. The description of the Level 0 data products below also applies to Level 0.5. Level 1 data are a browse product derived from the Level 0.5 data set. Level 2 data products will be derived from the Level 0.5 data set as the results of more advanced analysis.

5.1. LEVEL 0 DATA PRODUCT SET

Six data product types are delivered as MENA Level 0 data. These are listed in Table III and briefly described below. In view of the difficulty of species identification with MENA, we have selected a data reporting strategy that delivers as much raw data as possible for ground-based analysis, while still delivering some images for direct viewing.

The Image array elements are 8-bit representations of counts per accumulation that have been lossy compressed from 16-bits according to a pseudo-logarithmic scheme, such that 3% accuracy is retained for all 16-bit values. Image data products are by default subject to lossless compression in the CIDP. This can be changed by ground command.

5.1.1. *Statistics Data*

The raw FEE data, in addition to Sensor ID and spin phase, are reported for as many events as possible in the Statistics Data Product. Each event is reported as four bytes. These four bytes contain information as listed in Table 3. The number of bits reported for each quantity reduces the 8-bit knowledge available but retains sufficient resolution for our purposes. For example, eight degree resolution in polar angle requires a mean uncertainty in Start Position and Stop Position of 2 mm. The width of the Start anode segment is 11 mm and that of the Stop anode segment is effectively 73.5 mm. Thus one part in 5.5 and one part in 34 is the required resolution for the Start and Stop anode segments. This is provided by reporting 4 bits and 7 bits, respectively.

Statistics data packets contain up to 128 events. All events reported in a packet are acquired only from a single StartStop spin bin, which is identified in the packet header. The single bit provided in Statistics for Azimuth localizes an event to $\frac{1}{2}$ of a StartStop bin, increasing the effective reported azimuth resolution to 4 deg.

If there are more valid events in a spin than can be reported in the available telemetry (approximately 13 000 events per spin, assuming no lossless compres-

TABLE III
MENA data products

Image Data (counts per pixel)	
16 polar angles × 32 azimuth angles × 5 speeds × 3 sensors	
Statistics (Raw Front End Electronics Data; per event)	
Start position, 4 bits	
Start height, 6 bits	
Stop position, 7 bits	
Stop height, 6 bits	
Time of flight, 6 bits	
Fine azimuth, 1 bit	
Sensor ID, 2 bits	
StartStops Data (counts per pixel)	
Starts in 45 azimuth angles × 3 sensors	
Stops in 45 azimuth angles × 3 sensors	
Valid events in 45 azimuth angles × 3 sensors	
ENA – Viewing Error singles (Esingles; counts per pixel)	
Hardware error	(Illegal state machine condition)
TOF overflow	($T_{STOP} - T_{START}$ > preset threshold)
TOF underflow	($T_{STOP} - T_{START}$ > preset threshold)
Start height overflow	(Start_Sum> preset threshold)
Start ratio overflow	(Start_A/Start_Sum>preset threshold)
Start ratio underflow	(Start_A/Start_Sum< preset threshold)
Stop height overflow	(Stop_Sum > preset threshold)
Stop ratio overflow	(Stop_A/Stop_Sum> preset threshold)
Stop ratio underflow	(Stop_A/Stop_Sum< preset threshold)
Start-start	(Two consecutive Starts without an intervening Stop)

sion), Valid Event reporting in Statistics will be rationed. The rationing will be based on the distribution of Valid Events acquired during the previous spin.

TABLE III
Continued.

Anti-ENA-Viewing Error singles	
(Asingles; counts per pixel)	
Hardware error	(Illegal state machine condition)
TOF overflow	($T_{STOP} - T_{START} >$ preset threshold)
TOF underflow	($T_{STOP} - T_{START} >$ preset threshold)
Start height overflow	(Start_Sum> preset threshold)
Start ratio overflow	(Start_A/Start_Sum>preset threshold)
Start ratio underflow	(Start_A/Start_Sum>preset threshold)
Stop height overflow	(Stop_Sum > preset threshold)
Stop ratio overflow	(Stop_A/Stop_Sum> preset threshold)
Stop ratio underflow	(Stop_A/Stop_Sum< preset threshold)
Start-start	(Two consecutive Starts without an intervening Stop)
Housekeeping	(engineering data relevant to Instrument health and safety)

*Course azimuth (8 deg resolution) provided in Statistics data packet header. All events in packet share same coarse azimuth.

TABLE IV
Speed and energy bands for the MENA image data products

Minimum speed (km s^{-1})	Maximum speed (km s^{-1})	Nominal speed* (km s^{-1})	Nominal energy** (keV; H)
438	669	565	1.6700
656	1003.5	848	3.7540
984	1505	1271	8.4387
1476	2256	1906	18.969
2214	3382	2858	42.641

*RMS.
**Assumes hydrogen.

5.1.2. *StartStops Data*

Starts, Stops, and Valid Events from each sensor are accumulated in 16 bit counters which are read out and reset every eight degrees of spin phase. The three resulting 3×45 element count arrays are then lossy compressed down to 8-bits each and packetized for telemetry downlink.

5.1.3. *Singles Data*

Numerous conditions can result in failure to declare a valid event even though Start and/or Stop MCP pulses have been detected (and counted). Ten of these have

been identified and are reported separately for the ENA and anti-ENA segments of spacecraft spin (32 spin bins each). They are also reported separately for the three sensors, giving two Singles arrays of size (3, 32, 10). These singles data products undergo lossy compression, and are by default subject to lossless compression in the CIDP. This can be changed by ground command. The ten error conditions reported in Singles data are listed in Table III.

5.1.4. *Housekeeping Data*

Data relevant to engineering concerns and health and safety are reported in 212 bytes of housekeeping data every spin. In view of the 2-min spacecraft spin period, many quantities such as voltage and temperature are reported as maximum, minimum, and mean values observed during the spin. Housekeeping data enjoys the highest priority among data products for telemetry downlink. It is the only data product reported in the Low and High Voltage Science modes which may not be subjected to lossless compression in the CIDP.

5.2. LEVEL 1 DATA

MENA Level 1 data will be derived directly from the Image data products (A1, A2, and A3) described above. Data from the three sensors and the three or four largest speeds will be combined to form a single contiguous 2D image of ENA flux in units of #/(cm^2 sr s). This image will span the range of polar angles from 20 to 160 deg in 28 pixels, each 5 deg wide. There will be 32 pixels in azimuth, spanning the range of the ENA spin segment. By default, each azimuth pixel will be 4 deg wide such that the image will span the range from -64 to $+64$ degrees to either side of local nadir.

Figure 13 contains an example of the MENA level 1 browse product. The ENA fluxes shown here are generated from the ring current model of Fok et al. (1999) during a dipolarization event. Brief description of the ring current model and the simulation results of a substorm injection can be found in the deconvolution paper in this issue (Perez et al., 2000). Figure 13 shows the integrated ENA fluxes from the upper 3 energy channels of MENA. The left panel shows the image at the beginning of a geomagnetic dipolarization and the right panel at the end of the dipolarization. It can be seen that fluxes increase during the dipolarization (note that different scales for 2 panels) and the enhanced region propagates earthward in response to the inductive electric field.

These Level 1 images will be extracted from the Level 0.5 data at GSFC, using algorithms provided by the MENA science team, and formed into both GIF and CDF files. They will be distributed along with other IMAGE data products to the entire IMAGE science team. They will also be made available to the scientific community and the public both through the NSSDC and the GSFC IMAGE web site.

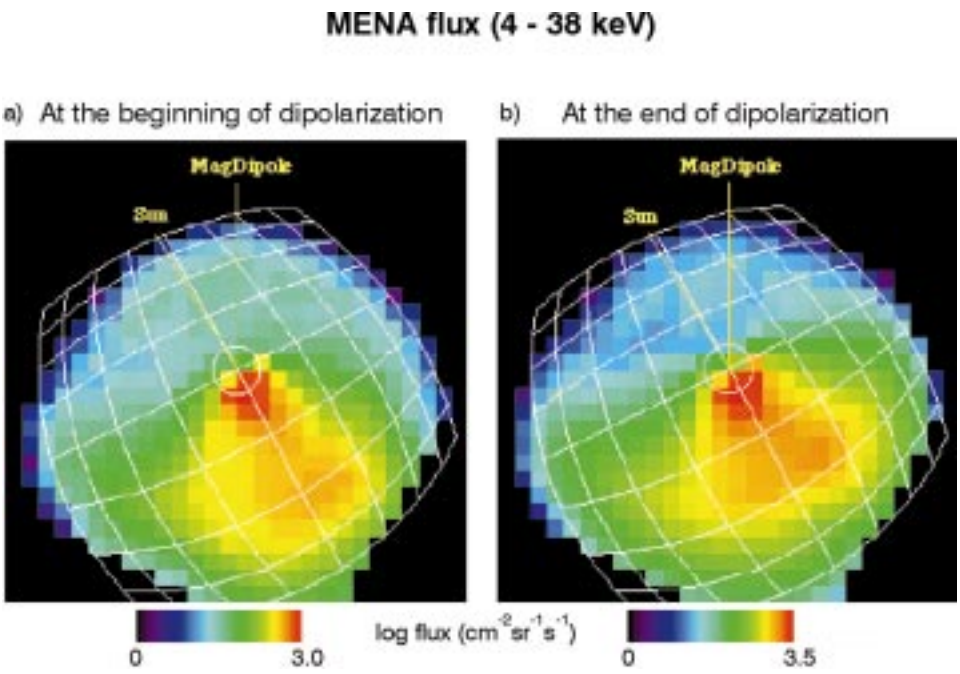

Figure 13. Simulated ENA images from a hypothetical instrument with characteristics similar to the MENA imager. These images are formed using a model for energetic ion fluxes before and after a large scale geomagnetic reconfiguration where the magnetosphere transitions from a state characterized by a stretched out tail (a) to one where the tail field lines are much more dipolar (b). The region of enhanced ENA flux is located on the anti-sunward portion of the magnetosphere. Directions of the magnetic dipole and to the sun are shown. The color bars scale the ENA flux and are different for the two cases (a and b).

6. Calibration

The MENA imager has undergone extensive calibration at several levels. All flight FEE (FEETOF and FEEPHA) and HVPS cards were calibrated on the bench at Southwest Research Institute (SwRI). All flight detector assemblies were calibrated using point UV illumination under high vacuum at the University of California at Berkeley. Every flight grating was characterized for UV and energetic particle transmission under high vacuum at the Los Alamos National Laboratory (Los Alamos). Each of the three flight sensors was calibrated under illumination by H^+, He^+, and O^+, incident from a variety of directions and with a variety of energies, under high vacuum at Los Alamos. End-to-end calibration of the MENA imager system, including all three sensors was conducted using both ions and ENAs under high vacuum at SwRI. A sampling of results from the end-to-end calibrations is given below.

6.1. POLAR ANGLE MEASUREMENT

ENA polar angle is derived from the MENA Start and Stop positions as given by Equation (1). Uncertainty in the polar angle (angular resolution) is derived from uncertainty in the Start and Stop positions as

$$|\delta\alpha| = \frac{\sin^2(\alpha)}{L}\sqrt{(\delta Z_p)^2 + (\delta Z_T)^2}\ , \tag{3}$$

assuming that errors in z_p and z_t are uncorrelated. This equation can be cast strictly in terms of Start and Stop positions with the following result:

$$|\delta\alpha| = L\sqrt{(\delta Z_p)^2 + (\delta Z_T)^2}/(L^2 + Z_p^2 - 2Z_pZ_T + Z_p^2)\ . \tag{4}$$

The task of polar angle calibration is to determine, for any pair of Start and Stop values, the most likely Start and Stop positions associated with the ENA, and the likely uncertainty in those positions. This information allows identification of the polar angle and its uncertainty according to Equations (1) and (4).

Polar angle calibration was accomplished by illuminating the aperture at a known location with a narrow beam, while acquiring and recording the Statistics data product. This was done at multiple locations and from multiple directions with a 31 keV proton beam, allowing a full range of known locations on the Start and Stop anodes to be sampled. A collimated broad beam was passed through a narrow (0.05 cm) slit upstream of the MENA imager, resulting in the pattern of aperture illumination sketched in Figure 14. Figure 14 shows a front view of a MENA sensor (without the collimator), overlaid with the footprint of the narrow slit calibration beam. At any given angle, the imager was translated such that the narrow beam was scanned across the narrow dimension of the aperture (up and down in the figure). Data was acquired at each position, providing samples across the full range of Start positions and a small (1 cm) range of Stop positions for a single polar angle. Executing this routine at various polar angles allowed the entire Stop anode segment to be calibrated. *A priori* knowledge of the beam position within the aperture was not required, since decreases in count rates at the aperture edges on either side provided this information.

Figure 15 shows summary data from a single polar angle acquired in this manner. All data are plotted versus position in the chamber (different from sensor) frame of reference. StartStop count rates are plotted in the top three panels. Localization of counts to within the aperture is apparent. The five bottom panels display spectrograms of the five raw FEE bytes, reported in the Statistics data product as described above. The top two panels among these five show the Start Height and Start Position byte distributions. The Start position byte distributions vary across the range as the position is incremented. The next two panels show the Stop Height and Stop Position byte distributions. The Stop Position byte also varies with position, but not across the entire range since this plot displays data acquired at a single

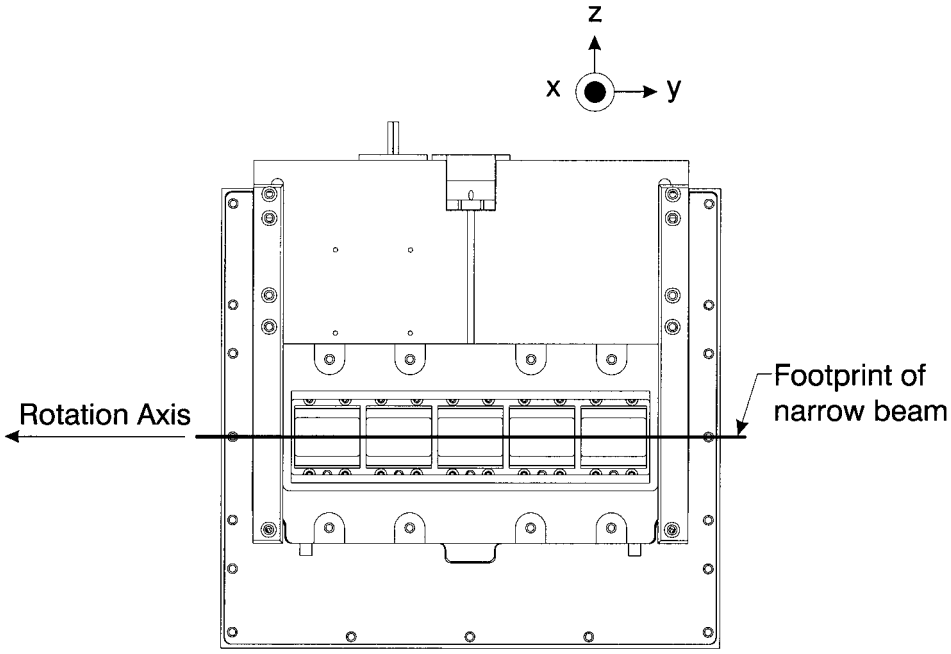

Figure 14. Sketch of the footprint of narrow calibration beam upon the MENA aperture. A narrow beam (black line) illuminates the complete width of the aperture for a given, fixed elevation angle. For clarity, the aperture is shown without collimators. This pattern could be scanned across the aperture (in z-direction), while independently controlling the polar incidence angle.

polar angle. The TOF byte distribution displayed in the bottom panel shows values localized to approximately 40, appropriate for this 31 keV proton beam.

Figure 16 shows a map of calibration points on the Sensor 2 Start and Stop anode segments obtained in this manner. Though the displayed dimensions are actually parallel, and not physically orthogonal to one another, this display format provides an effective summary of the coverage obtained. The horizontal lines show the inner and outer limits of the two Stop anode segments. Note that groups of data points lie along lines slanted slightly upward to the right, which are groups obtained at constant polar angles.

Samples of Start and Stop Position byte distributions obtained in the experiments described above yield the data shown in Figures 17(a) and 17(b), respectively. In each, we have performed a least squares Gaussian fit to the distribution. The logarithmic plot of the data reveals non-Gaussian characteristics of the distributions at first order and below. The blind spot in Stops is evident in Figure 17(b) between byte values 128 and 174. The small peak in the Stops near bin 120 is an artifact which will be removed from the raw data in software.

Summaries of data such as that shown in Figure 17 are shown in Figure 18. Here we show fitted gaussian centroids of the Start and Stop Position byte distributions versus position within the aperture for Starts (Figure 18(a)), and versus

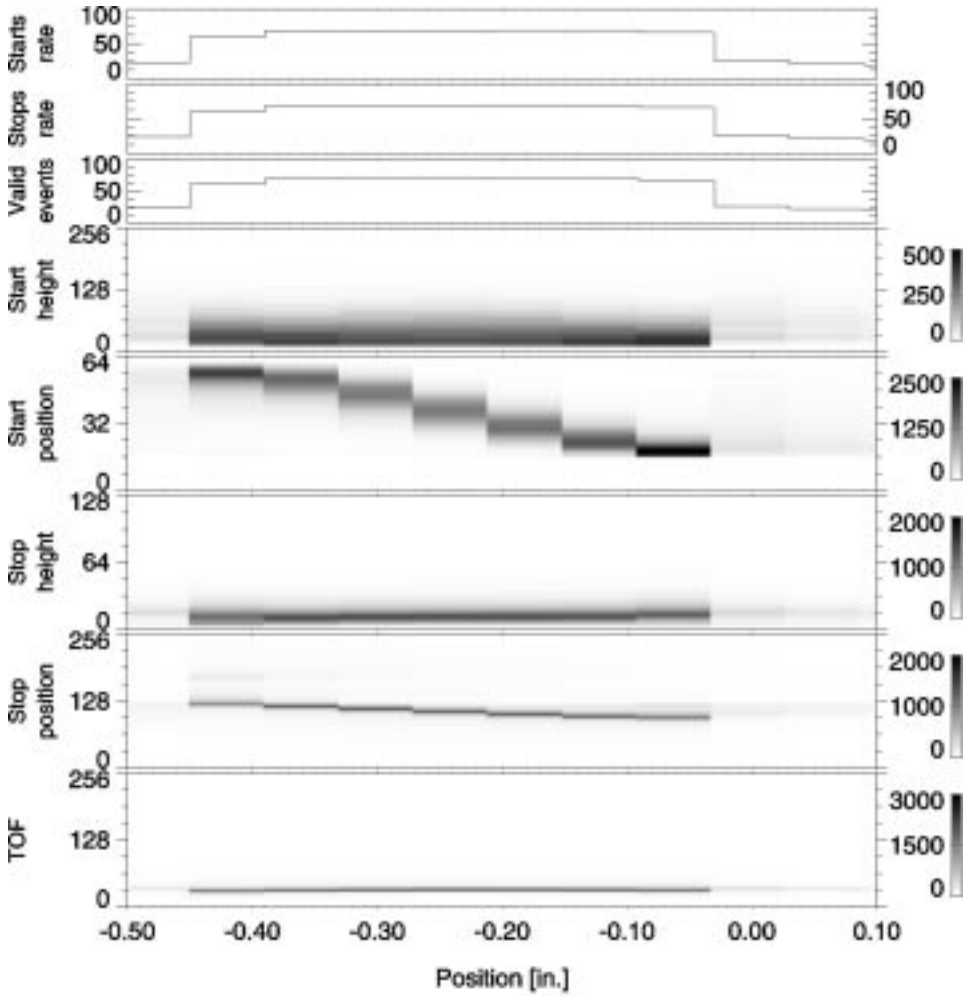

Figure 15. Stack plot of MENA sensor 2 narrow slit calibration data. The top three panels show StartStop count rate data (Starts, Stops, and Valid Events). The lower five panels provide spectrograms of the five raw front-end electronics bytes. The grey scale represents count rates, as functions of position and byte value. The position axis represents z-coordinate of the narrow beam footprint (refer to Figure 14) in the frame of reference of the calibration chamber.

position projected geometrically onto the Stop anode segment in the case of Stops (Figure 18(b)). The error bars represent FWHM of the distributions, derived from the fitted Gaussian widths. The linear response of the system is evident. In the Stops distributions, the error bars expand near the edges of the anode segments. Completion and synthesis of this type of analysis for the entire data set represented in Figure 16 for all three sensors will be required to form images from the data obtained once IMAGE is in orbit.

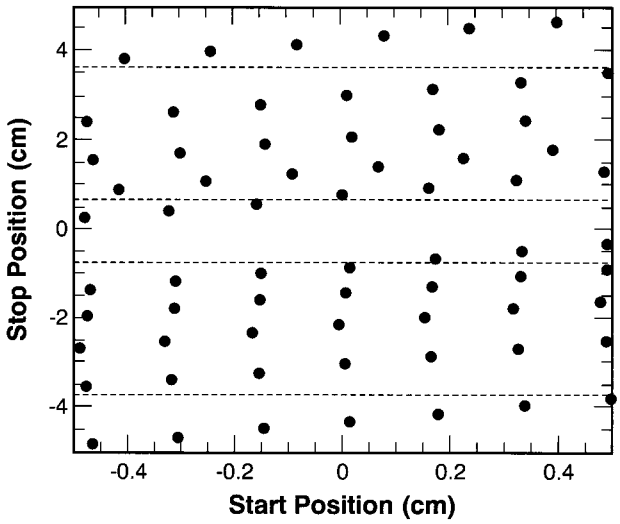

Figure 16. Map of the narrow slit calibration coverage for MENA sensor 2. Dashed lines indicate the inner and outer limits of the two Stop anode segments.

The analysis just outlined addresses only a single mass at a single energy – and a high energy case at that. ENAs with larger mass and smaller energy will yield similar results with larger error bars because of scattering within the foils, as discussed earlier. The MENA calibration data set includes sufficient energy and mass sampling to quantify this effect.

6.2. TIME-OF-FLIGHT CALIBRATION

Data were acquired in the calibration laboratory using species, energies, and polar angles sufficient to sample a wide range of times-of-flight (TOF) for all three sensors. TOF byte distributions from the Statistics data product have been analyzed for a small portion of that data. The results are summarized in Figure 19. Here we plot the mean value of TOF byte versus expected TOF based on the input ENA energy, mass, and angle of incidence. The large error bar associated with the data point near 160 ns TOF is due largely to energy and angular scattering of the 3.9 keV O beam. Though we have not yet analyzed the calibration data, we fully expect to observe similar smearing in the polar angle distributions for this species and energy. These high mass, low energy data show the limitations of the current technology.

6.3. SENSITIVITY AND FIELD OF VIEW

A simple method was used to measure the absolute sensitivity and limits on the MENA imager fields of view. The entire aperture was illuminated with a collimated broad beam of known flux from a wide range of directions spanning the 2D field of view. Under these circumstances, the ratio of the Valid Event rate reported in

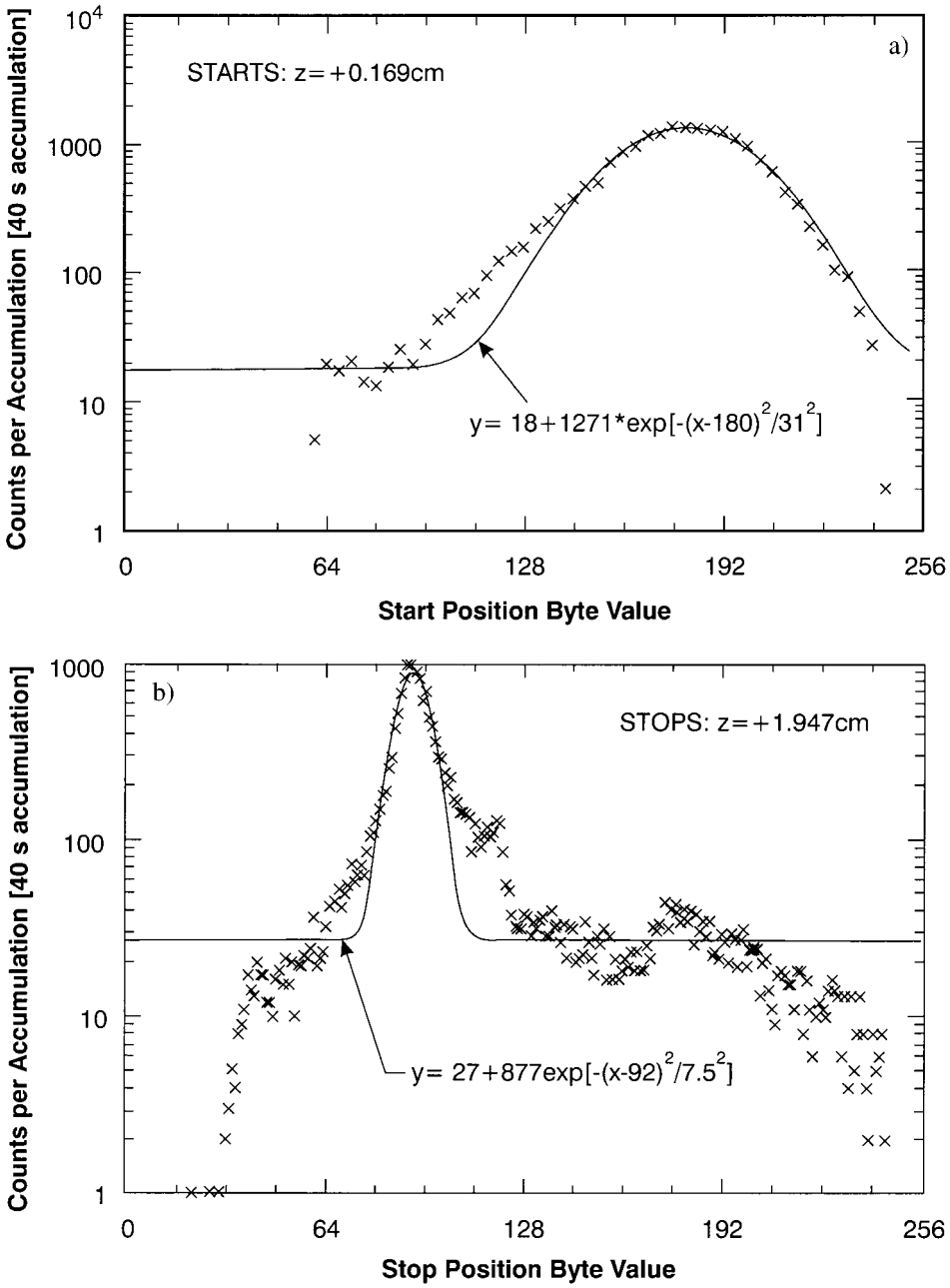

Figure 17. Histograms of count rates in the Start (a) and Stop (b) position bytes from a single position in the narrow slit calibration.

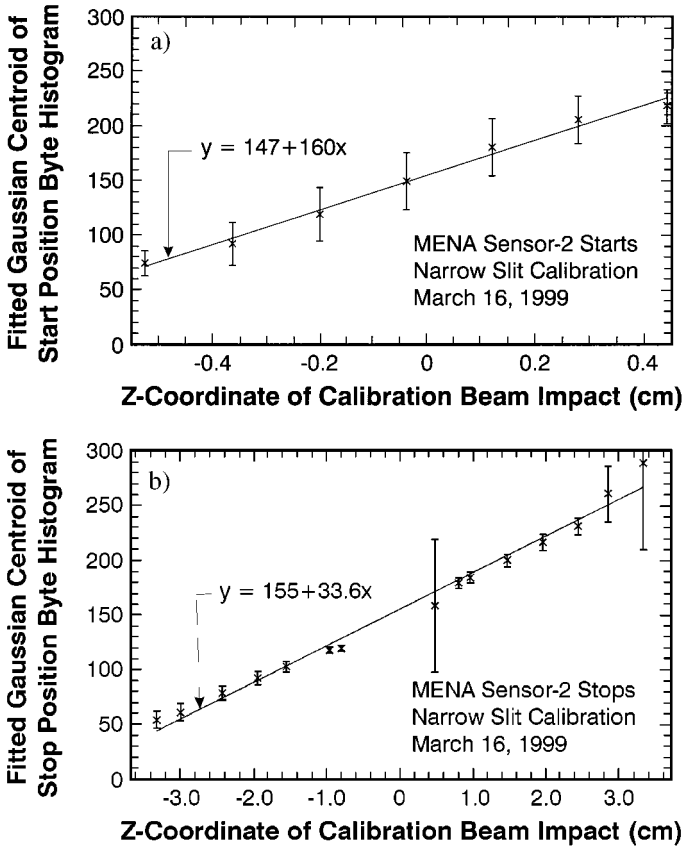

Figure 18. Fitted Gaussian centroids for Start (a) and Stop (b) position byte distributions plotted versus the measured z-coordinate of the narrow beam footprint within the aperture for Starts, and the nominal z-coordinate of ENA impact on the detector for Stops. Error bars are derived as FWHM using the fitted Gaussian widths.

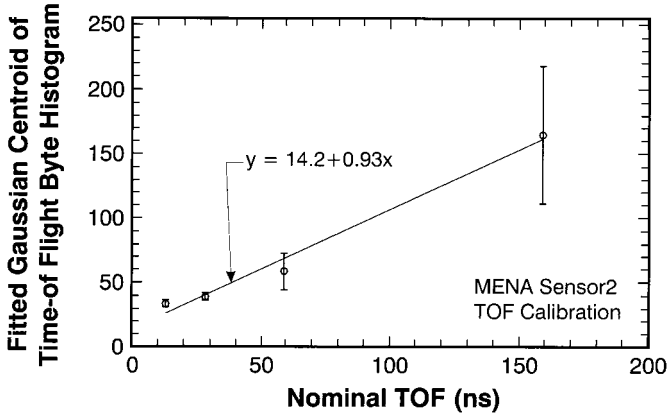

Figure 19. Fitted Gaussian centroids for TOF byte distributions plotted versus nominal time of flight for an incident calibration beam. Error bars are derived as FWHM using the fitted Gaussian widths.

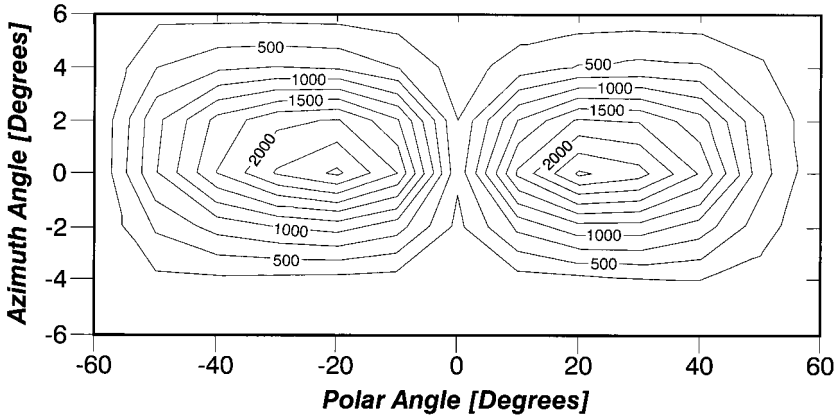

Figure 20. MENA imager valid event rate in Hz for exposure of a single sensor to a broad beam from a wide range of azimuth and elevation angles.

the StartStops data product to the magnitude of the incident flux yields a direct measure of the sensor effective area as a function of both polar angle and azimuth angle. Displays of this quantity in the case of Sensor 2 are contained in Figure 20. Integral moments of this distribution, approximated using numeric sums, provide the single sensor geometric factor in units such as cm^2 sr. They also provide the size of the fields of view in azimuth and polar angle. Figures 21(a) and 21(b) display preliminary results of analysis of data such as that in Figure 20. Note that the polar angles plotted in Figure 21 are in the vacuum chamber frame of reference, which is offset from the Sensor 3 frame of reference by 20 degrees. Figure 21(a) shows effective area plotted differentially with respect to polar angle for MENA flight Sensor 3. The effective area for this single sensor maximizes at a value $\sim$0.175 cm^2 near polar angles of 12 deg with respect to sensor normal. Figure 21(b) demonstrates that the FWHM azimuthal field of view (and resolution) varies somewhat with sensor polar angle but has a mean value near 5 degrees.

7. Ground System

MENA data will be processed to Level 0.5 and distributed along with spacecraft orbit and attitude (OA) data, and other ancillary data in Universal Data Format (UDF) (Gurgiolo, 2000) to IMAGE team institutions. The distribution medium will be digital video diskette (DVD). At SwRI, the data will be ingested and placed online on two redundant servers. Both servers will provide identical data structures but different default client interfaces. One server will provide data access and browse products through a web interface to the general scientific community. The other will serve the MENA science team at SwRI and elsewhere. In the event one server is disabled, the other will provide both functions until the situation is rectified. The entire MENA data set will remain online for the duration of the IMAGE mission.

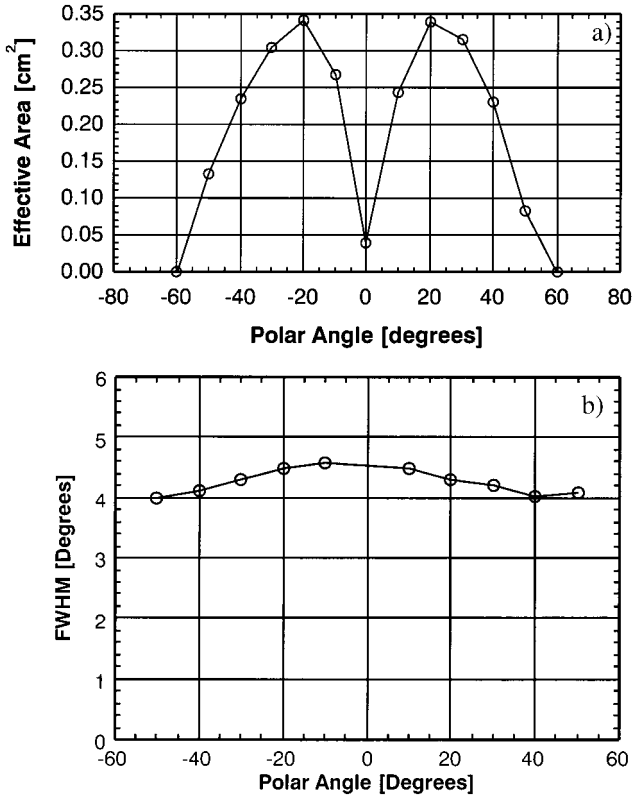

Figure 21. Subsets of the data shown in Figure 20. (a) shows sensor effective area at a single azimuth angle. (b) shows the second integral moment (with respect to azimuth) of the distribution in Figure 20. This result is interpreted as the FWHM of the azimuth (spin) angle pass band. Both quantities are plotted as a function of incident polar angle.

8. Summary

The MENA imager, together with the other scientific instruments on IMAGE, is poised to provide the data upon which breakthrough scientific understanding can be achieved regarding our planetary magnetosphere and ionosphere. Global scale observation of magnetospheric response to the solar wind driver will foster intuitive understanding of system properties.

In this paper we have described the goals and broad objectives of the IMAGE/MENA project. We have described the MENA imager and its principles of operation, and have shown examples of measured component and instrument level performance. We have described instrument data products and, briefly, the ground data system. The reader hopefully has gained an understanding of what we are trying to accomplish, how we are going about it, and a vision of how the MENA and other imager data sets can contribute to the study of magnetospheric physics.

The simulated images in Figure 13 provide a realistic forward-looking estimate of what one might see when looking at the magnetosphere through MENA eyes. The transition from stretched (pre-substorm) to more dipolar (after expansion phase) tail configuration is reflected in the ENA images. Note that the image on the left is more elongated anti-Earthward (stretched tail), while that on the right is less so; the emitting region is more bulbous in the case of the post expansion phase magnetosphere on the right. The tail has unloaded. The geomagnetic field has undergone a dipolarization (Fok et al., 1999). The electric current supporting the stretched tail field has been diverted and/or undergone collapse. The result of this process is the 'snap' to a more dipolar configuration. Details of global scale energetic ion transport and ion energization associated with this global transition in magnetic topology will be revealed, as in this demonstration (Figure 13).

The challenges of neutral atom imaging and other forms of large-scale global system sampling are only now dawning on the global scientific and technical community. For ENA imaging, the low flux level is a determining constraint. As the geocoronal density falls off with Earth-centered radial distance, the ENA production rate per energetic ion falls off proportionally. Signal levels from the high-altitude magnetosheath, the down-tail plasma sheet, and magnetopause or near-tail reconnection sites are typically quite low for this reason. This can be overcome by deploying future imagers with large effective area, or by employing long accumulation periods (untenable for studying dynamic processes).

It is interesting and useful to conjecture about what we will observe and learn with IMAGE, and about how future generations of ENA imagers will evolve. Standing on the shoulders of authors cited and others, we anticipate the MO/DA phase of IMAGE with curiosity and optimism.

Appendix A

The MENA imager is designed for a two-year mission aboard the IMAGE satellite. This program is one of NASA's Medium-class Explorer missions. As such, all electrical and electronic parts are required to meet Grade 3 or better screening levels. Electronics on the IMAGE satellite are expected to accumulate a total dose of 30 krad (Si) behind 0.200″ aluminum walls. Parts used for MENA electronics meet a design goal of 60 krad (Si) total dose or else they have extra shielding.

The total mass of the MENA imager is 13.9 kg. It requires 0.8 A of 28 V spacecraft power for normal operations. The instrument maintains isolation from the spacecraft power bus. It uses RS-422 differential signaling to communicate with the spacecraft. All instruments on the IMAGE satellite are required to pass MIL-461C EMI tests. MENA passed all aspects of the EMI testing with no waivers required.

The MENA imager is composed of three identical sensor heads, positioned at offset angles to reduce the effects of the blind-spot that is inherent to the sensor

design. To service the sensor heads, there are three identical sets of front-end electronics. The front-end electronics include a high voltage power supply (HVPS), a pair of Charge Amplifiers (CHAMPS), a time of flight board (FEETOF), and a pulse height analysis board (FEEPHA). These three sets of front end electronics are operated using the four other boards in the instrument: the look-up table board (LUT), the high voltage and pulser control board (HVPC), the central processing unit board (CPU), and the low voltage power supply board (LVPS).

The sensor requires three different high voltage supply levels. A $+4$ KV supply is used to power the micro-channel plates (MCPs). A $+10$ KV supply is required for the collimator plates to sweep out ions. A -1 KV supply provides an acceleration potential for secondary electrons from the carbon foil. Each sensor head is supplied by its own independent High Voltage Power Supply board (HVPS).

Each HVPS is a single circuit board ($4.8'' \times 5.3''$) that provides 3 outputs ($+4$ KV, $+10$ KV, and -1 KV). There are actually two -1 KV outputs on each board and they are diode OR-ed together to provide redundancy. The $+4$ KV output produces more than 54 μA at full voltage, the $+10$ KV output produces more than 12 μA at full voltage, and the -1 KV output produces more than 35 μA at full voltage.

The HVPS boards are very robust. The outputs are 'zap trapped' to provide a protective current path if an arc should occur in the load. The supplies safely drive a dead short indefinitely and have a small overshoot ($<10\%$) on short circuit recovery. The outputs of the HVPS may be shorted to ground while at full voltage without damaging the supplies. Finally, the HVPS boards are parylene coated for additional protection. Parylene is a conformal coating with a very high dielectric strength.

The CHAMPS are a high speed, discrete design. A JFET input stage is followed by a pair of RF transistors for current gain. Then a shaping network produces a bipolar pulse. An operational amplifier in the final stage has high gain in the narrow frequency band of the bipolar pulse and is capable of driving the coaxial output cable. The CHAMPS are adjusted to provide a gain of 0.15 V/pC. Their noise floor is 0.6 mV r.m.s. and their maximum output without any distortion is 7 V.

The CHAMPS also perform a summation of the A and B wedges of the anode. Each CHAMP provides an A and an A+B output. This output is the most convenient form for processing by the FEETOF and FEEPHA boards. The amplitude of the sum, A+B, is not modulated by location on the anode and is therefore useful for TOF work and to determine total charge.

The bipolar pulses are used to prevent a shift up in the baseline when there is a pileup of pulses. This would affect the accuracy of the pulse height analysis and the accuracy of our position measurement. The zero crossing of the bipolar pulse occurs at a fixed time after every MCP charge dump. Like a pendulum, the zero cross time is theoretically independent of pulse height. In practice the variation is very small and provides an excellent way to determine TOF using a simple zero crossing circuit.

The FEETOF and FEEPHA have a board to board connector that allows them to work as a single unit. Both boards' circuitry is held in reset until the Start Sum signal exceeds the minimum threshold that has been set by software command. Once the threshold has been broken, a fast, low dispersion comparator (AD9696) is used to detect the zero crossing of the Start Sum bipolar pulse. This signal is used to steer a 6 mA constant current source into a 2000 pF polycarbonate capacitor (M87217/01). A similar circuit is used to process the Stop Sum signal, which is used to steer the constant current source away from the 2000 pF capacitor. A 15 nS delay is inserted into the path of the Stop Sum signal so that the circuit turn on and turn off times don't cause non-linearities for small times-of-flight. The voltage on the 2000 pF capacitor is digitized by an A/D converter (7672RP) and then subsequently cleared. The times-of-flight that the FEETOF measures range from 5 nS to 350 nS.

The FEEPHA detects the peak of all four signals from the CHAMP: Start (A), Start Sum (A+B), Stop (A), and Stop Sum (A+B). These peaks are held and any noise inputs during the conversion process will not corrupt their values. An analog divider is used to divide the Start signal by Start Sum Signal to create the Start Position signal. An analog divider is also used to create the Stop Position Signal. The analog dividers are given time to settle and then the results are digitized by A/D converters (7672RP). The Start Sum and Stop Sum signals are also digitized to yield Start Height and Stop Height.

The FEETOF and FEEPHA then signal that a valid event has been acquired. The event is read out and processed by a state machine that is running inside a field programmable gate array (FPGA) on the LUT board. Besides valid events, the FEETOF and FEEPHA check for several error conditions. These include: Start event followed by a second Start event, Ratio overflow, Ratio underflow, Start Sum overload, Stop Sum overload, Time-to-Amplitude (TAC) underflow, and TAC overflow. In order to decrease the dead time of the front end electronics, some of these errors cause the conversion cycle to be immediately terminated. This reduces our susceptibility to noise caused by UV photons. Another piece of diagnostic information that the FEETOF board sends down to the LUT board is the raw Event Start and Event Stop digital signals that are generated every time the threshold is broken. This allows the system to determine total count rates without any masking caused by the dead time.

The Look-Up Table board (LUT) processes all of the events that are generated by the three sensor heads. When a valid event has occurred, the LUT board reads out the data from the FEETOF and FEEPHA that captured it. Then it clears the FEETOF and FEEPHA to re-arm them to capture the next event. There are five bytes of raw data which are read from the front end electronics: time-of-flight, start position, start height, stop position, and stop height. The LUT cascades these raw bytes through a series of look-up tables that are stored in EEPROM (electrically erasable programmable read only memory). In principle, these tables allow the instrument to compute the angle, speed, species, and energy of the ENA that caused

the event. This information, along with the spin angle of the spacecraft, is used to form a seventeen-bit event address into the science image memory. The event count at this address is then incremented. This process can be used to form an array of images with each image in the array corresponding to a different species and energy range, though in practice we form the Image data product assuming Hydrogen; species determination will be pursued in the ground based analysis, using the Statistics data product. The science image memory is double buffered so that one spacecraft spin of data can be collected while the previous spin's data is being transferred. The LUT also counts the error events and total starts and total stops so that these can be transferred down in the telemetry data. Finally, the LUT passes the raw data bytes from the front end electronics to the CPU so that it can collect statistics data. This data path allows us to pass the raw events down in our telemetry data.

The CPU board uses an RTX2010 micro-controller. Its job is to execute the commands that are received from the spacecraft and to process instrument science data into packets and transmit it to the spacecraft. It performs a lossy 16-bit to 8-bit compression on the science images using a look-up table. The CPU board also collects and reports housekeeping data. The data communication between the instrument and the spacecraft is done over RS-422 signal lines. The spacecraft provides pulses to the CPU that allow it to monitor the spin of the spacecraft and determine nadir as well as the location of the Sun. The CPU uses this information to periodically dip the voltage on the MCPs when they are about to have direct exposure to the Sun. The processor's code is stored in EEPROM so that it can be modified while on orbit.

Acknowledgements

This paper and the work it describes could not exist without the dedicated efforts of countless individuals at many levels. The many contributors include Rudy Abeyeta, Janice Anderson, Tom Booker, Pat Casey, Michelle Chippie, Kathy Coers, Ken Cook, Dan Everett, Bob Fleming, Carrie Gonzalez, Pat Gonzalez, Brian Gupta, Ron Harper, Pat Hindle, Ernest Mayfield, Bill McLaren, John McLeod, Greg Palacios, Norm Pelletier, Benny Piepgrass, Jane Prentiss, Adrian Ramirez, Syrrell Rogillio, Dorothy Rosales, John Rudzki, Y. Saito, James Sanders, Mary Sattler, Tony and Norma Sawka, Stanley Silvus, Kirk Smith, Brian Stone, Jack Taguiam, Glenda Waters, Edie Wilson, and Dave Young. The authors appreciate useful conversations with Steve Fuselier, Don Mitchell, Joe Perez, and Ed Roelof on the topic of ENA imaging, Dave Slater and Ossy Siegmund regarding detector function, and innumerable others from whom good advice was given. This work was supported at SwRI under NASA Contract NAS 5-96020. Work at the Los Alamos National Laboratory was carried out under the auspices of the U. S. Department of Energy with financial support from the NASA IMAGE Program. Work

at MIT, UCB, and WVU was performed under subcontract to SwRI. Work at the University of Southern California was performed under subcontracts from SwRI and Los Alamos.

References

Balkey, M. M., Scime, E. E., Schattenburg, M. L. and van Beek, J.: 1998, 'Effects of Gap Width on EUV Transmission Through Sub-Micron Period, Free-Standing Transmission Gratings', *Applied Optics* **37**, 5087–5092.

Fok, M.-C., Moore, T. E. and Delcourt, D. C.: 1999, 'Modeling of Inner Plasma Sheet and Ring Current During Substorms', *J. Geophys. Res.* **104**, 14,557–14,569.

Frank, L. A., Craven, J. D., Ackerson, K. L., English, M. R., Eather, R. H. and Carovillano, R. L.: 1981, 'Global Auroral Imaging Instrumentation for the Dynamics Explorer Mission', *Sp. Sci. Instrum.* **5**, 369–393.

Frank, L. A., Craven, J. D., Burch, J. L. and Winningham, J. D.: 1982, 'Polar Views of the Earth's Aurora with Dynamics Explorer', *Geophys. Res. Lett.* **9**(9), 1001–1004.

Funsten, H. O., McComas, D. J. and Barraclough, B. L.: 1993, 'Ultrathin Foils Used for Low Energy Neutral Atom Imaging of Planetary Magnetospheres', *Opt. Eng* **32**, 3090–3095.

Gibson, W. C. et al.: 2000, 'The IMAGE Observatory', *Space Sci. Rev.* **91**, 15–50 (this issue).

Gurgiolo, C.: 2000, 'The IMAGE High-Resolution Data Set', *Space Sci. Rev.* **91**, 461–481 (this issue).

Gruntman, M. A: 1995, 'Extreme Ultraviolet Radiation Filtering by Freestanding Transmission Gratings', *Appl. Opt.* **34**, 5732–5737.

Gruntman, M. A.: 1997, 'Energetic Neutral Atom Imaging of Space Plasmas', *Rev. Sci. Instrum.* **68**, 3617–3656.

Hall, L. A.: 1985, 'Solar Ultraviolet Irradiance', in A. S. Jursa (ed.), *Handbook of Geophysics and the Space Environment*, Air Force Geophysics Laboratory.

Mauk, B. H. and Meng, C.-I.: 1983, 'Characterization of Geostationary Particle Signatures Based on the 'Injection Boundary' Model', *J. Geophys. Res.* **86**(A4), 3055–3071.

McComas, D. J., Funsten, H. O. and Scime, E. E.: 1998, 'Advances in Low Energy Neutral Atom Imaging', in R. Pfaff, J. Borovsky and D. T. Young (eds), *Measurement Techniques for Space Plasmas (Fields)*, American Geophysical Union, Washington, AGU Monograph 103, 275–280.

McComas, D. J., Funsten, H. O., Gosling, J. T., Moore, K. R., Scime, E. E. and Thomsen, M. F.: 1994, 'Fundamentals of Low-Energy Neutral Atom Imaging', *Opt. Eng.* **33**(2), 335–341.

McComas, D. J., Barraclough, B. L., Elphic, R. C., Funsten, H. O. III and Thomsen, M. F.: 1991, 'Magnetospheric Imaging with Low-Energy Neutral Atoms', *Proc. Natl. Acad. Sci.* **88**, 9598–9602.

Meier, R. R.: 1991, 'Ultraviolet Spectroscopy and Remote Sensing of the Upper Atmosphere', *Space Sci. Rev.* **58**, 1–186.

Mende, S. B. et al.: 2000, 'Far Ultraviolet Imaging From the IMAGE Spacecraft: 1. System Design', *Space Sci. Rev.* **91**, 243–270 (this issue).

Mitchell, D. G. et al.: 2000, 'High Energy Neutral Atom (HENA) Imager for the IMAGE Mission', *Space Sci. Rev.* **91**, 67–112 (this issue).

Moore, T. E., Arnoldy, R. L., Feynman, J. and Hardy, D. A.: 1981, 'Propagating Substorm Injection Fronts', *J. Geophys. Res.* **86**, 6713.

Moore T. E. et al.: 2000, 'Low Energy Neutral Atom (LENA) Imager for the IMAGE Mission', *Space Sci. Rev.* **91**, 155–195 (this issue).

Perez, J. D., Fok, M.-C. and Moore, T. E.: 2000, 'Deconvolution of Energetic Neutral Atom Images of the Earth's Magnetosphere', *Space Sci. Rev.* **91**, 421–436 (this issue).

Ritzau, S. M. and Baragiola, R. A.: 1995, 'Electron Emission from Thin Carbon Foils by keV Ions', *Phys. Rev. B* **44**, 2529–2538.

Scime, E. E, Anderson, E. H., McComas, D. J. and Schattenburg, M. L.: 1995, 'Extreme-Ultraviolet Polarization and Filtering with Gold Transmission Gratings', *Appl. Opt.* **34**, 648–654.

Van Beek, J. T. M, Fleming, R. C., Hindle, P. S., Prentiss, J. D., Schattenburg, M. L. and Ritzau, S.: 1998, 'Nanoscale Freestanding Gratings for Ultraviolet Blocking Filters', *J. Vac. Sci. Technol.* **B16**(6), 3911–3916.

Williams, D. J., Roelof, E. C. and Mitchell, D. G.: 1992, 'Global Magnetospheric Imaging', *Rev. Geophys.* **30**(3), 183–208.